V. GRAVITATION RESEARCH*

Academic and Research Staff

Prof. R. Weiss
Dr. D. J. Muehlner
R. L. Benford

Graduate Students

D. K. Owens
N. A. Pierre
M. Rosenbluh

A. BALLOON MEASUREMENTS OF FAR INFRARED BACKGROUND RADIATION

1. Introduction

The discovery in 1965 of the isotropic cosmic background radiation by Penzias and Wilson[1] and its subsequent interpretation by Dicke et al.[2] as the red-shifted remnant of the thermal radiation of a primordial cosmic fireball opened one of the most fascinating areas in observational cosmology.

Gamow,[3] in the early 1950's, in his work on the origins of the universe had alluded to this radiation but had not stressed the fact that it might be observable. This is probably the reason why his calculations had been forgotten by 1965.

Ground-based measurements[4,5] in the region 0.1-3 cm^{-1} have been consistent with the interpretation that the universe is filled with blackbody radiation at 2.7°K. Extensive measurements[6,7] of the isotropy of the radiation at 0.33 cm^{-1} have lent additional support to the cosmic hypothesis.

Although the existence of an isotropic microwave background radiation is well established, the crucial questions of whether the spectrum is truly thermal and whether the radiation is indeed isotropic in the region where it has maximum spectral brightness remain unanswered.

The spectral peak of a 2.7°K blackbody lies at approximately 6 cm^{-1}. This is a miserable region of the electromagnetic spectrum in which to carry out experiments. The technology of far infrared detection is in a primitive state; furthermore, even if this situation eventually improves, background measurements in this region will be complicated by the inevitable radiation from sources that are at temperatures considerably higher than 3°K.

Radiation by the Earth's atmosphere is sufficiently strong to preclude direct

*This work was supported in part by the Joint Services Electronics Programs (U.S. Army, U.S. Navy, and U.S. Air Force) under Contract DAAB07-71-C-0300, and in part by the National Aeronautics and Space Administration (Grant NGR 22-009-526) and the National Science Foundation (Grant GP-24254).

ground-based measurements in the region above 3 cm^{-1}. This leaves the field to balloon, rocket or spacecraft observations, or to the use of indirect techniques such as measurements of the distribution of rotational states of interstellar molecules by absorption spectra of the interstellar medium.[8, 9]

Since 1967 several groups have carried out direct measurements in this region[10-14] using rocket and balloon-borne instruments.

This report describes a balloon experiment designed to make a direct measurement of the background radiation in the 1-20 cm^{-1} region and presents results of two balloon flights made on June 5, 1971 and September 29, 1971, from the balloon facility of the National Center for Atmospheric Research (NCAR), Palestine, Texas.

2. Apparatus

The design of a balloon-borne radiometer to make an absolute measurement of the isotropic background spectrum in the far infrared is constrained in several ways. First, radiation from the optical components of the radiometer should not greatly exceed the incoming radiation. In practice this means that all optical components must be held at liquid-helium temperatures. In fact in this experiment the optical apparatus is immersed in liquid helium.

A second constraint is imposed by the poor detectors that are available for the far infrared region. For example, a detector with an area of ~0.1 cm^2 is typically able to detect a minimum of ~10^{10} photons in one second. The optics must therefore have as large a solid angle-area product as is practical; in the apparatus described in this report it is approximately 0.3 cm^2 sr.

At the same time the radiometer beam must be narrow enough in angle to permit measurements of atmospheric radiation by zenith angle scanning and also small enough in cross section to enter the liquid-helium dewar without being intercepted by surfaces at ambient temperature. The opening in the dewar cannot be made very large without incurring prohibitive losses of liquid helium.

A typical flight may last one-half day during which time the instrument must remain immersed in liquid helium. This is ensured by enclosing it in a sealed copper can surrounded by a reservoir of liquid helium which is allowed to evaporate into the atmosphere, thereby providing refrigeration. The liquid helium in the sealed can is used only as a thermal conductor. Because liquid helium shrinks by a remarkable 15% between 4.2°K and 1.5°K, the entrance window to the radiometer can is recessed so that it will always be in contact with the liquid.

Finally, some provision must be made to separate the atmosphere at low altitudes from the liquid helium, since otherwise the radiometer would be covered with air frost and water frost. This separation is provided by two gas-tight transparent covers which are removed during the course of the experiment. A schematic drawing of the apparatus

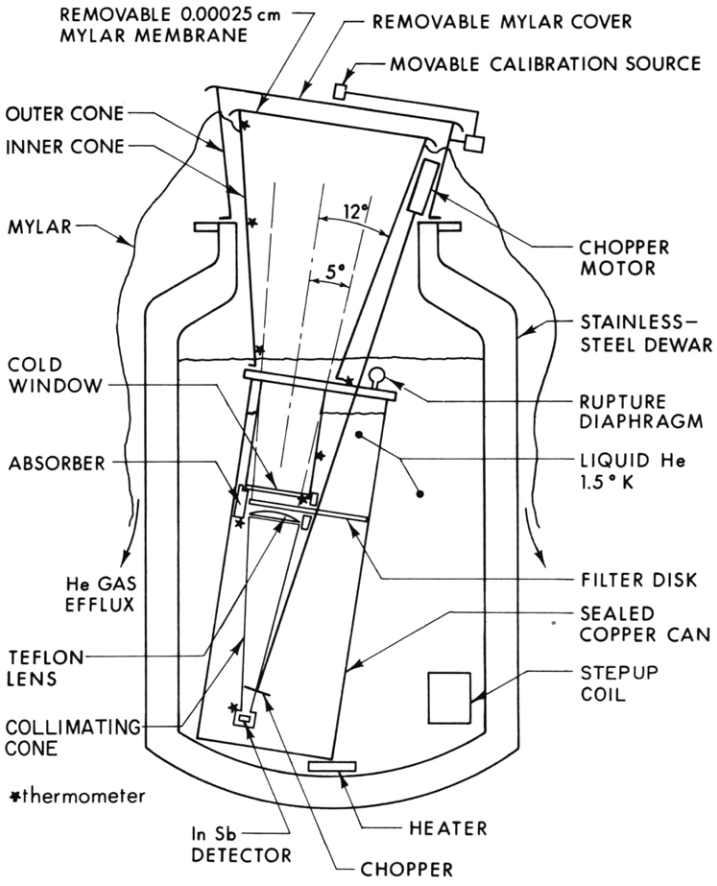

Fig. V-1. The apparatus.

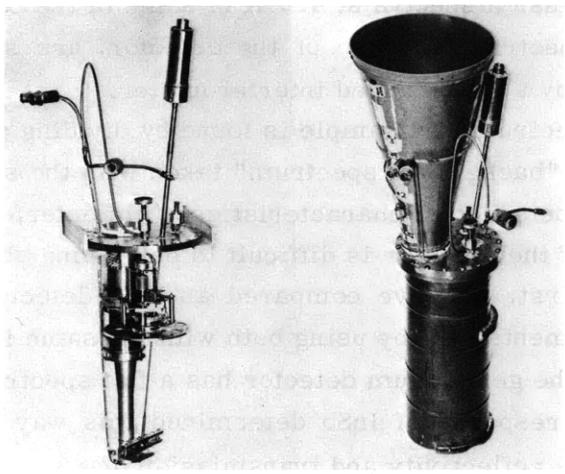

Fig. V-2. Radiometer.

is shown in Fig. V-1.

The principal optical components of the radiometer (Fig. V-2) are the cold window, the interference filters, the Teflon lens, the collimating cone, the beam chopper, and the detector. The optical properties of these components are described below.

Collimation of the radiometer beam is accomplished by a cone-lens combination, which is composed of an aluminum condensing cone with a Teflon lens mounted at the top. The lens is designed to have its focal point at the vertex of the cone. In the limit of geometric optics[15, 16] the cone-lens system is an ideal condenser of radiation; it illuminates the lower opening with radiation from a full 2π solid angle while accepting radiation at the upper opening only from the solid angle allowed by energy conservation. In other words, it is an f/0 condensing system which conserves the solid angle-area product of the beam passing through it. The major constraint on the design of the cone is the size of the detector, which fixes the diameter of the lower opening. The size of the upper cone opening is determined by the best compromise between beam diameter and divergence. The cone used in the experiment has a lower opening, 0.5 cm in diameter, and an upper opening of 5.5 cm. The beam half angle is ~5° by geometric optics.

A filter disk with 6 evenly spaced openings is located above the collimating cone. One of the six openings is filled with a transparent Teflon sheet, 4 openings are occupied by lowpass interference filters, and the sixth position is blocked off by a sheet of copper. Any of the six filter positions may be selected by rotating the disk, which is turned by a rotary solenoid operating in the liquid helium. An absorber composed of iron-filled epoxy surrounds the radiometer beam in the region of the filter disk and blocks off indirect paths by which scattered radiation might bypass the filters.

Far infrared transmission spectra at 4.2°K of some of the components in the optical train, as well as the spectral response of the detector, are shown in Fig. V-3. All spectra were measured by a far infrared interferometer.

The transmission spectrum of a sample is found by dividing a spectrum taken with the sample in place by a "background spectrum" taken with the sample removed. The ratio is not affected by the spectral characteristics of the interferometer and detector. The spectral response of the detector is difficult to determine absolutely. We have used several approaches. First, we have compared an InSb detector with a germanium bolometer (Texas Instruments Co.) by using both with the same interferometer. It is generally assumed that the germanium detector has a flat spectral response in the far infrared. The spectral response of InSb determined this way is shown in Fig. V-3. Second, we measured the reflectivity and transmission of a sample of InSb at 4.2°K. The reflectivity is frequency-independent while the transmission increases with frequency. Under the assumption that the power absorbed is proportional to the signal developed, these measurements will give the spectral response of the detector. The

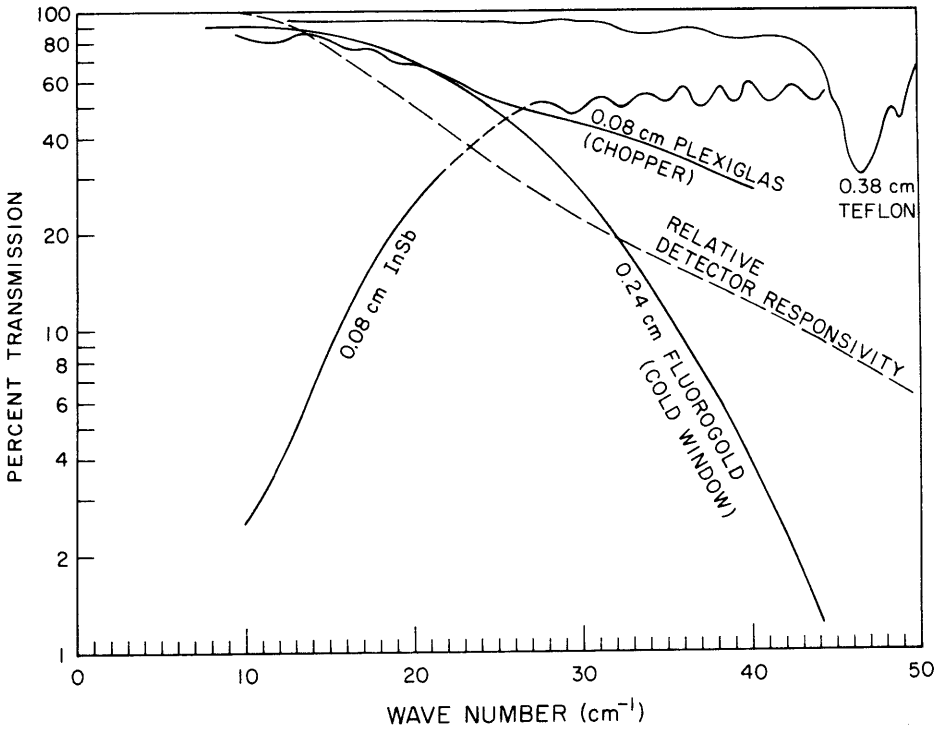

Fig. V-3. Transmission spectra at 4.2° of some optical components of the radiometer. The relative detector responsivity vs frequency is shown, as well as the transmission spectrum of a sample of the InSb detector material.

results are consistent with the spectrum found by comparing the InSb and germanium detectors. Finally, the blackbody calibration of the entire instrument appears to confirm the adopted detector response.

The dominant high-frequency roll-off for the instrument is determined by the cold window and the detector response. The cold window is opaque from ~40 cm^{-1} on through the visible region of the spectrum. Spectral resolution is provided by a set of capacitive grid, lowpass interference filters similar to those described by Ulrich.[17] A detailed account of the construction of rugged filters of this kind which can be used at low temperatures has been given in a previous report.[18]

The low-frequency cutoff of the instrument is due to the collimating cone. The cutoff frequency of the cone is too low to be easily measured directly, and so the approach that we took was to measure the cutoff characteristics of small-scale models of the actual cone. We found, as expected, that these cones exhibited sharp cutoffs at frequencies inversely proportional to the sizes of the cones. The cutoff of the cone used in the experiment is at ~1 cm^{-1}.

The five spectral responses of the entire instrument are shown in Fig. V-4. SR1 is

composed of the product of the spectral response of cold window, collimating cone, Plexiglas chopper, and detector. SR2 through SR5 are obtained by multiplying SR1 by the appropriate interference filter transmission spectra.

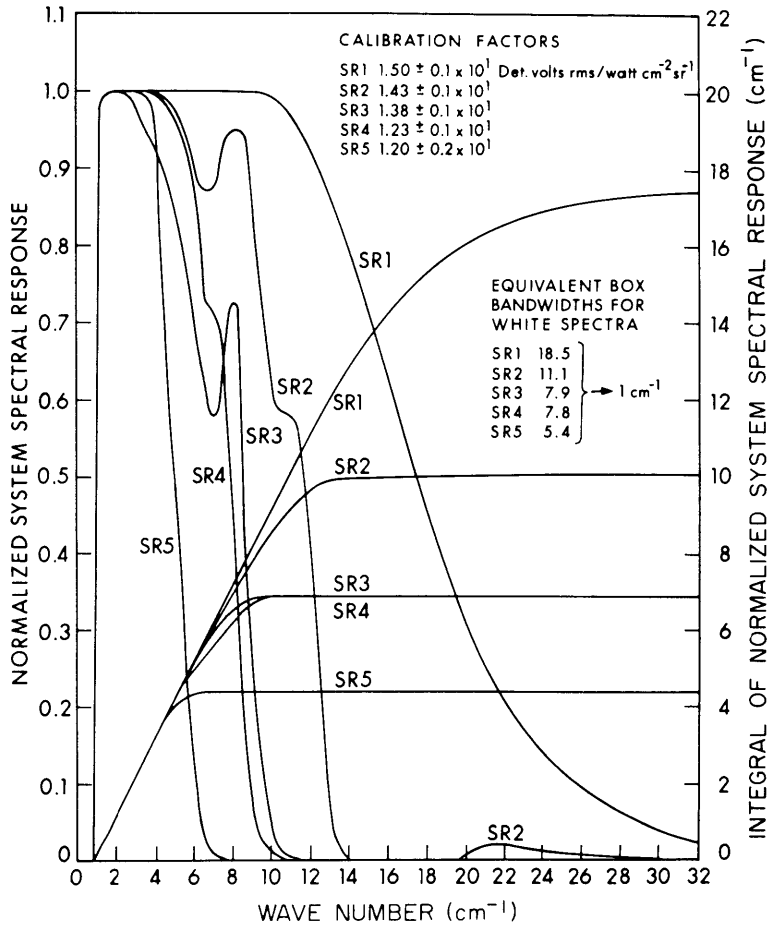

Fig. V-4. Five spectral responses of the instrument.

The response curves are normalized at low frequencies. The vertical axis may be calibrated for each spectral response by multiplying by the calibrated factor shown in Fig. V-4.

Figure V-5 shows the same five responses multiplied by the frequency squared, and shows better than Fig. V-4 how the instrument responds to high-temperature thermal source spectra. The "equivalent box bandwidths" listed in both Figs. V-4 and V-5 show the high-frequency cutoffs of ideal square box filters which would give the same response to white and ν^2 spectra as the actual responses SR1-SR5.

The beam profile of the radiometer was measured with the instrument in its flight

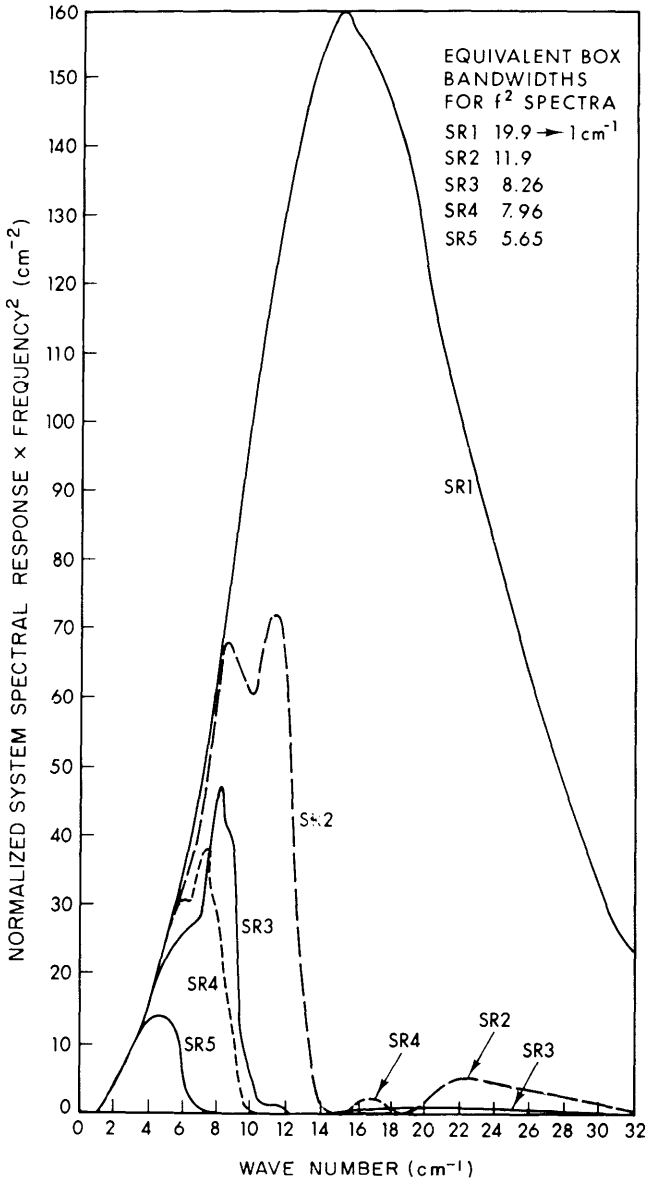

Fig. V-5. Spectral responses multiplied by the frequency squared.

configuration except that a sheet of polyethylene, 0.005 cm thick, was substituted for the mylar membrane and cover. The measurement was carried out by moving a modulated mercury arc source across the radiometer field of view at a distance of ~2 1/2 m from the cold window. The beam profile of the radiometer measured in this manner for each spectral response is shown in Fig. V-6. It is evident that the angular distribution depends on the spectral response; the radiometer beam widens with decreasing cutoff frequency. This appears to be a diffraction phenomenon which probably occurs in the collimating cone. The polyethylene sheet also causes a systematic broadening

of the angular distribution which, unlike the diffraction broadening, increases with increasing frequency. This comes about by multiple reflections of the radiometer beam between the polyethylene sheet and the conical radiation shield at the entrance to the radiometer. Since all of the covers are removed during the flight, the angular distributions shown in Fig. V-6 give upper limits for the weak large-angle tails of the actual distributions.

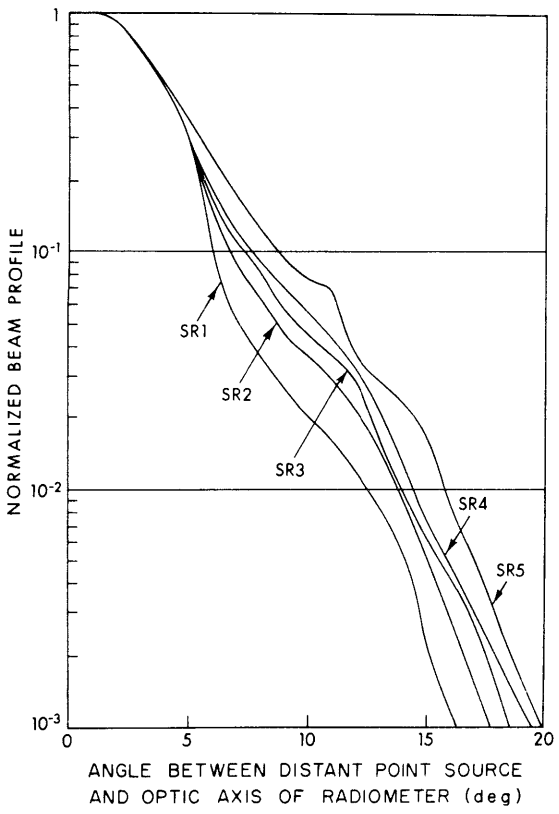

Fig. V-6.
Radiometer beam profile in each of the spectral responses.

Figure V-7, which is derived from the data of Fig. V-6, shows the response of the radiometer to a ring source of constant linear intensity everywhere at an angle θ to the optic axis, as well as the integral of this quantity from 0 to θ. The limiting value of the integral may be interpreted as the effective solid angle of the radiometer beam in each spectral response; note that the values tabulated for these "effective solid angles" depend on the normalization of the point source response to unity at $\theta = 0$, as shown in Fig. V-6.

Since the radiometer beam does not have a sharp cutoff, it is necessary to shield the radiometer from hot sources at large angles. In particular, the radiometer should not see any reflections of the hot ground and lower atmosphere. Inadequate precautions in this respect may have been the most serious flaws in the 1969 flight of the first apparatus.[14] The main purpose of the inner cone shown in Fig. V-1 is to ensure that only the sky will be reflected into the radiometer at large beam angles. Furthermore, it is necessary to minimize the thermal emission of radiation by the cone itself.

The cone extends from a region at ambient temperature to the top of the sealed can which is at liquid-helium temperature. In order to minimize the heat flow into the dewar, the cone is constructed of 0.013 cm stainless steel, a metal of high emissivity. To reduce its emissivity, the cone is gold-plated and then coated with a layer of Teflon, 0.01 cm thick. This dielectric layer reduces the emissivity at grazing angles, which for bare metal surfaces is dramatically larger than at normal incidence. The calculated emissivity of the cone over the frequency range of the radiometer is less than

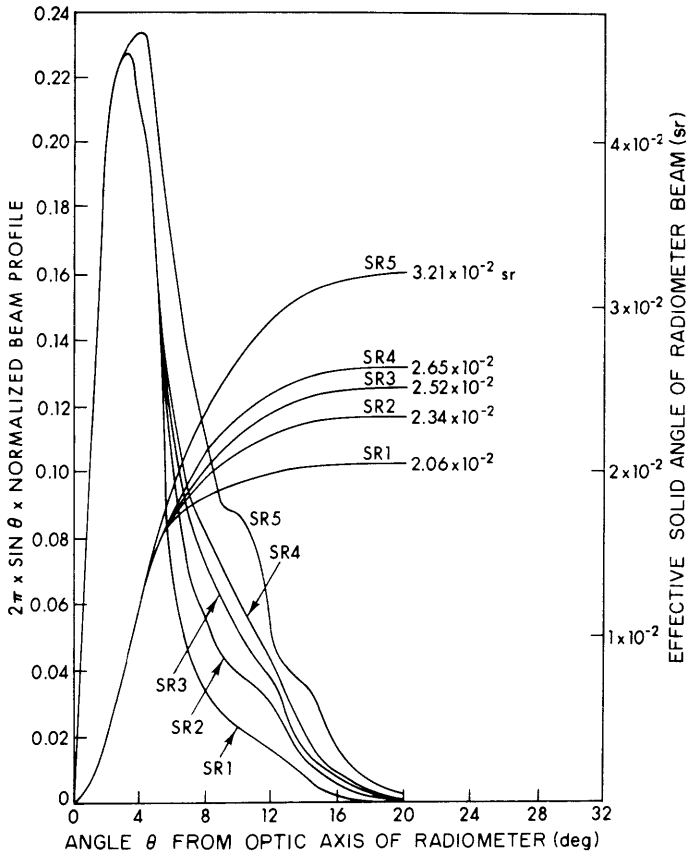

Fig. V-7. Annular response and the effective solid angle within θ vs θ.

0.0025 at all angles.

In order to estimate the cone's contribution to the radiometer signal, it is necessary to know what fraction of the total beam is intercepted by the cone in each spectral response. This was measured by moving a modulated mercury arc source across the radiometer beam at a height level with the top of the cone, but with the cone removed. The results are 0.92%, 2.5%, 2.15%, 3.15%, and 6% for SR1-SR5. The top of the cone has a diameter of 26 cm.

In order to keep out of the instrument contaminants such as moisture, dust, ballast, and air, it is protected by two sheets of mylar which cover the opening at the top. The covers are stretched on hoops mounted by spring-loaded hinges and may be flipped out of the way of the radiometer beam by burning through nylon fastening lines. The outer cover is a sheet of mylar, 0.0025 cm thick, which makes a gas-tight seal to the outer cone. This cover stops the bulk of the moisture, dust, and ballast, and is removed early in the flight. The inner cover, or membrane, is mounted in the same way as the outer cover. It is a sheet of mylar, 0.00025 cm thick, and forms a gas-tight seal to the top of the inner cone. The membrane serves to keep air out of the instrument both during the ascent and at float. More will be said about it in the description of a flight.

An important requirement for the covers is that they be transparent in the far infrared so that measurements can be made during the ascent, and so that in the event of failure of the cover-release mechanism a flight would not be a total loss. In an investigation of cover materials we measured the absorption length in thick sections of mylar and polyethylene at 300°K in the spectral region characteristic of SR1. The absorption length in polyethylene was ~8 cm, and for mylar it was ~0.3 cm. From these measurements the emissivities of the mylar cover and membrane are calculated as 8×10^{-3} and 8×10^{-4}. Radiation arising from reflection of the dewar and cone by the cover and membrane is negligible compared with emission. In the June 5, 1971 flight we used polyethylene covers, but we experienced some difficulties. In the September 29, 1971 flight we used mylar because of its superior mechanical properties.

The detector used in the experiment is an InSb hot-electron bolometer which was first described by Rollin.[19] Detectors were cut on a string saw from a boule of undoped n-type InSb, with the following specifications at 77°K: carrier concentration, $6 \times 10^{13}/cm^3$; Hall mobility, 5×10^5 $cm^2/V\text{-}s$; and resistivity, 0.3 Ω cm. After being cut into chips of approximately $5 \times 5 \times 1/2$ mm, detectors were etched in a standard CP-4 solution. Gold leads were attached to the chips, with indium doped with sulfur or tellurium used as solder. The assembled detectors were tested for their responsivity and noise characteristics. In the course of these studies, we found some simple criteria for bad detectors. Detectors which displayed asymmetric V vs I curves with current reversal, or had unusually high impedances, generally proved to be noisy. Non-ohmic or otherwise poor contacts are probably responsible for this.

A good detector usually had a dynamic resistance of 100 Ω or less at the optimum operating point, which was usually at bias currents between 0.1 mA and 0.5 mA and near the knee of the V vs I curve. A good detector shows no increase in noise when the bias current is turned on. The V vs I curves at 4.2°K and 1.8°K for the detector used in the radiometer are shown in Fig. V-8.

A major problem with InSb detectors, because of their low impedance, is to match them to amplifiers so that the amplifier noise is less than the thermal noise generated in the detector. At present, the best field-effect transistors such as the 2N4867A used in the detector preamplifier typically have a voltage noise of $\sim 5 \times 10^{-9}$ $V/Hz^{1/2}$, and a current noise of $\sim 5 \times 10^{-15}$ $A/Hz^{1/2}$ at frequencies above 100 Hz. The thermal noise of a 100 Ω InSb detector at 4°K is approximately 2×10^{-10} $V/Hz^{1/2}$. Using a liquid-helium-cooled setup transformer is a straightforward way to make the impedance transformation. Unfortunately, we found that ferromagnetically coupled transformers and inductors are microphonic and their windings have a tendency to break on thermal cycling. We use a series RLC step-up circuit employing a 2.7 H air-core inductor wound with copper wire on two nylon dees. The dees are arranged as sections of a toroid to reduce pickup from external magnetic fields. The coil is enclosed in a superconducting

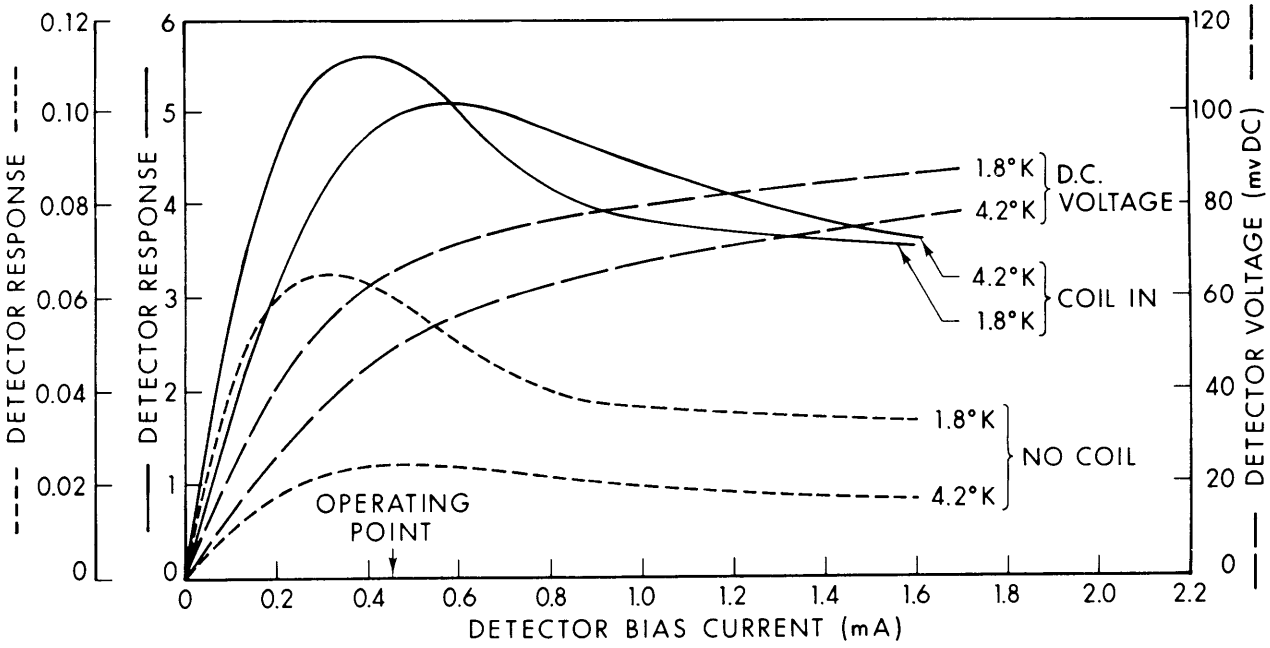

Fig. V-8. Detector bias voltage and responsivity vs bias current. Curves labeled "coil in" include the voltage step-up because of the RLC circuit at 2.1 kHz chopping frequency; curves labeled "no coil" show the response of the detector without the RLC circuit.

magnetic shield and potted in mineral oil to reduce microphonics. The tuning capacitor is across the FET preamplifier input. The Q and therefore the voltage setup of the RLC circuit is 50. The overall noise voltage of the system with the chopper turned off is roughly twice the thermal noise of the detector at 4°K.

Figure V-8 shows the synchronously detected output signal of the detector when irradiated by a modulated mercury arc as a function of the bias current. The curves at 4.2°K and 1.8°K both show responsivity vs bias current with and without the step-up RLC circuit. They display the increase in detectivity with decreasing temperature, as well as the loading of the detector by the RLC circuit.

At 1.5°K the responsivity is ~200 V peak to peak per watt incident on the detector. Under the assumption that the detector noise is twice the 4°K thermal noise, the detector has a noise equivalent power of $\sim 2 \times 10^{-12}$ W/Hz$^{1/2}$.

The final element of the optical train which deserves some comment is the chopper. The chopper is a Plexiglas disk, 0.75 mm thick, divided into 22 wedge-shaped sections, with alternate sections aluminized. The disk, driven by an external synchronous motor, rotates at 30 Hz in a slot cut into the collimating cone 1.5 cm above the detector. The chopper exposes the detector alternately to incoming and thermal radiation in a closed cavity at the helium bath temperature. A frequency reference signal is derived from the

chopper drive shaft near the motor.

In order to overcome the 1/f noise in the preamplifier, as well as to allow small electrical components to be used in the step-up and amplifier circuitry, it is desirable to use as high a chopping frequency as possible; however, this aggravates the substantial microphonics problem created by the chopper moving in the liquid helium. The chopper rim speed exceeds the critical velocities in superfluid helium by several orders of magnitude. Even in the normal fluid the chopper creates a flow with a very high Reynolds number, thereby producing turbulence. Since the signals to be measured are of the order of 10^{-9}-10^{-10} V, such things as the vibration of leads in the Earth's magnetic field and the change in capacitance of coaxial lines because of vibrations generate objectionable noise voltages if they are not controlled. While InSb is both piezoresistive[20] and piezoelectric,[21] it seems most likely that the dominant microphonic signals come from the temperature fluctuations accompanying pressure fluctuations in the liquid helium. The detector is mounted in a completely enclosed volume to reduce these fluctuations. We have not been completely successful in eliminating the microphonics problem. The microphonic noise remains the dominant noise in the experiment, and is approximately from 5 to 10 times larger than the thermal noise.

In the construction of the apparatus we have used various commercially available devices and materials which may be useful to others involved in cryogenic technology. Among these were the following.

"Fluorogold" (Fluorocarbon Company, Pinebrook, N.J.), the material used as the cold entrance window of the radiometer, is glass-filled Teflon which serves both as a lowpass filter in the far infrared and as a gasket for vacuum seals at cryogenic temperatures.

Chempro "O" rings (Chemical and Power Products, Inc., Cranford, N.J.), which can best be described as screen door springs enclosed in Teflon tubing, make reliable and thermally recyclible vacuum seals between smooth surfaces.

Cajon (Cajon Company, Solon, Ohio) fittings using replaceable nickel gaskets are useful for making seals that have to be opened or closed while at liquid-helium temperatures.

"Bartemp" stainless-steel ball bearings (Barden Corporation, Danbury, Conn.) operate well at low temperatures. Lubrication for the bearings is provided by Teflon ball separators impregnated with molybdenum disulfide. We use them to mount the chopper disk and in a gimbaled bearing located near the middle of the chopper shaft to prevent whipping of the shaft.

Ledex rotary solenoids (Ledex, Inc., Dayton, Ohio) operate well in liquid helium without alterations. In conjunction with Torrington one-way clutches (The Torrington Company, Torrington, Conn.), which have to be degreased before use, the rotary solenoids make simple stepping motors.

The 330-Hz detector signal, after passing through the low-noise preamplifier, is amplified further and converted into a dc output voltage in the conventional way by a lock-in amplifier. The noise bandwidth of the amplifier is determined by the output filter which provides a double integration with a time constant of 2 s.

An automatic way of accommodating the more than three-orders-of-magnitude signal variations which occur in the flight is provided by a gain switch which selects one of 7 discrete gains, covering a total range of a factor of 1000 in steps of $\sqrt{10}$. The switch is controlled by the lock-in amplifier output voltage and changes the gain when the output becomes less than 0.2 V or greater than 0.9 V for several seconds. The system is linear at any gain setting.

The radiometer dewar is attached to the frame of the balloon package (see Fig. V-11) on two pillow blocks. By means of a gear motor, the zenith angle of the radiometer beam may be varied between ~1° and ~45°. The zenith angle of the radiometer beam is measured by a pair of pendulous accelerometers fixed to the dewar. In this way the angle with respect to true vertical is measured irrespective of the orientation of the rest of the balloon package. The azimuth of the radiometer beam is not controlled; it is measured by a pair of Hall probes that sense the components of the Earth's magnetic field in two orthogonal directions.

A small blackbody used to monitor the performance of the radiometer during a flight is located at the top of the dewar assembly. This "inflight calibrator" is a conical piece of iron-filled epoxy of the same type as the laboratory calibrator. Its temperature is not controlled, but is measured by a wide-range resistor-thermistor combination. The blackbody is suspended by 3 thin wires at the center of a U-shaped hoop of thin-walled stainless-steel tubing large enough to clear the radiometer beam. The whole assembly is mounted on a velocity-controlled rotary solenoid which, when activated, moves the blackbody into the center of the radiometer beam. The position of the inflight calibrator is read out by a potentiometer mounted with the rotary solenoid.

A motor-driven camera is mounted on a post near the back of the balloon package and overlooks the top of the dewar. The camera is equipped with 12 flashbulbs for illuminating the apparatus during the darkness of a night flight, and can take that many pictures on 35-mm film.

The information gathered throughout the flight is telemetered to the ground, as well as recorded on an onboard tape recorder. One multiplexed channel carries the most essential information coming from the instrument, such as lock-in amplifier output, gain setting, filter position, zenith angle, azimuth, calibrator temperature and position, and various temperatures in the dewar. Another multiplexed channel carries housekeeping information. A multiplex commutation cycle lasts 15 s and is divided into 30 sections. The radiometer output is sampled every 1.5 s, which yields an essentially continuous record.

3. Calibration

Given the spectral response curves shown in Fig. V-4, a single measurement of the response of the radiometer in each spectral response, using a known source spectrum, would constitute a complete calibration of the instrument. In other words, this would fix the vertical scale of Fig. V-4 in volts per unit flux for each spectral response. Our faith is not that strong, however, and so we calibrated the instrument by exposing it to blackbody radiation over a wide range of temperatures down to ~3°K. Figure V-9 is a schematic drawing of the blackbody used for this calibration. The calibrator is immediately above the cold window through which the radiometer looks out at the world. The part of the calibrator which is actually black is a cylinder of iron-filled epoxy (Eccosorb MF-110, Emerson and Cuming, Inc.) with a conical hole in it. Measurements made on this material at 4.2°K with a far infrared interferometer showed it to have a reflectivity of approximately 10% between 10 cm^{-1} and 60 cm^{-1}, and also to be a strong absorber in thicknesses characteristic of the piece in the calibrator. The Eccosorb blackbody is matched to the radiometer by an aluminum cone, which optically magnifies it so that it almost completely covers the radiometer beam. The Eccosorb is mounted in a thick-walled OFHC copper "oven" which is heated by 10 resistors symmetrically arranged in holes in the copper, and cooled by the cold helium gas in the dewar. The temperature is measured by a carbon resistor thermometer, which was calibrated through a continuous range of temperatures determined by helium vapor pressure below 4.2°K, and by a commercial germanium resistance thermometer above 4.2°K. Both thermometers were checked at the discrete reference points provided by the boiling points of helium, hydrogen, nitrogen, and oxygen. The oven is insulated from the aluminum cone by a Teflon spacer. The temperature of the aluminum matching cone is never greater than that of the oven and, since aluminum is a good reflector, it has a negligible effect on the radiation seen by the radiometer.

Figure V-10 shows the reduced calibration data, in the form of detector voltage vs calibrator temperature. The solid curves are computer calculations based on the spectral responses of Fig. V-4. These curves are the frequency integrals of the spectral responses times the Planck blackbody spectrum at each temperature. The fit between the measured calibration points and the calculated curves has only one free parameter, the overall system gain, which is a common factor for all spectral responses.

The bulk of the calibrations were performed in a large environmental chamber at the Avco Corporation facility, in Wilmington, Massachusetts, in which the apparatus could be pumped down to a pressure of 2.5 mm Hg. At this pressure, which is equal to the pressure at flight altitude, liquid helium is at 1.5°K. For several reasons it is important to know how the response of the radiometer changes with helium bath temperature. For example, the preflight calibrations are performed at 4.2°K. Also, during

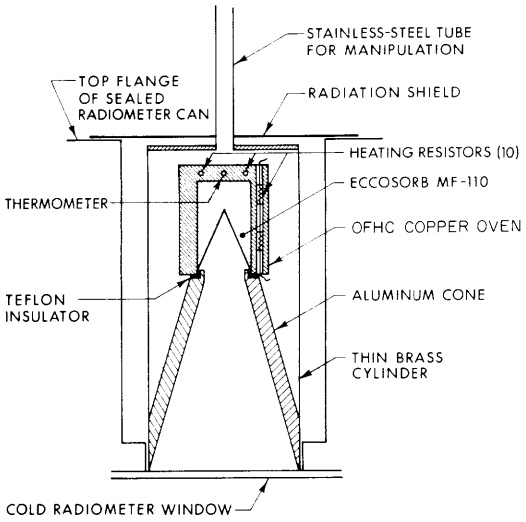

Fig. V-9.

Blackbody used for laboratory calibration of the radiometer.

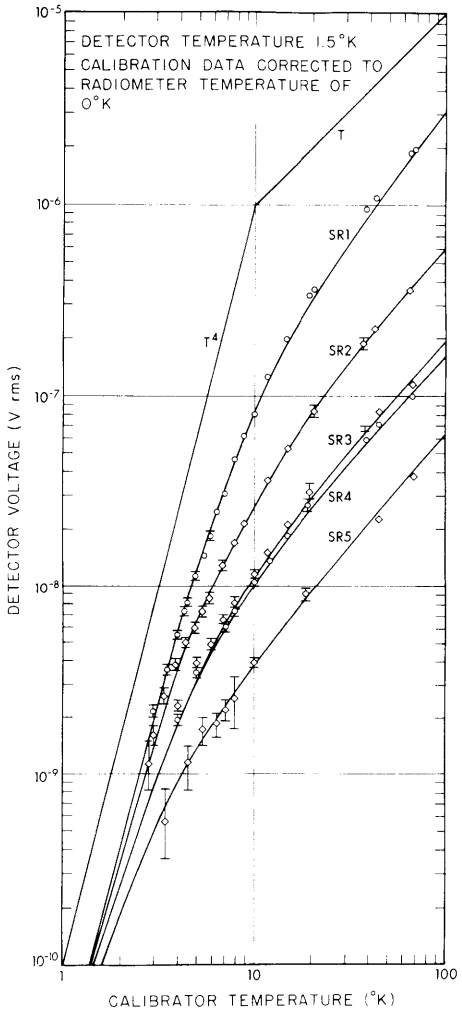

Fig. V-10.

Radiometer calibration curves.

the ascent the liquid-helium temperature changes continuously from 4.2°K to 1.5°K and finally, at the end of the flight, useful data can be obtained even though the apparatus may no longer be at 1.5°K. The bath temperature affects the calibration in two ways. First, the responsivity of the detector increases with decreasing temperature. Since the detector resistance also increases, the net effect when the loading of the RLC circuit is included is not large. The system gain increases by a factor of 1.4 between 4.2°K and 1.5°K. It is important to note that the measured spectral response of the InSb remains unchanged between these temperatures.

The second effect is more subtle. The ac detector signal is proportional to the difference between the power absorbed by the detector when the chopper is open and when it is closed. When the chopper is closed the detector is bathed in radiation at the temperature of the radiometer as determined by the liquid-helium bath. The observed signal attributable to an outside radiation source is therefore smaller than it would be for a radiometer at zero temperature. Indeed, if the temperature of the outside source were equal to that of the radiometer, no signal would be developed, and for an even colder source the signal would reverse phase. The dependence of the detector signal on the radiometer temperature is given by

$$V_{det.} \propto \int R(\nu) \left[B_{out}(\nu) - B_{rad.}(\nu, T)\right] d\nu,$$

where $B_{rad.}$ is the spectral brightness of a blackbody at the radiometer temperature T, B_{out} is the spectral brightness of the exterior source, and $R(\nu)$ is the spectral response function of the radiometer.

The most useful way to correct measured data for different radiometer temperatures is first to reduce the calibration data to an idealized radiometer temperature of 0°K, as illustrated in Fig. V-10. This procedure requires some trust in the measured spectral responses. The correction that should be added to the signal because of an outside source with the radiometer at a temperature T can now be read off the calibration curve for each spectral response directly.

A final problem in interpreting the calibration data is that the Eccosorb as reflected in the calibrator cone did not quite fill the whole radiometer beam. Consequently, when an actual measurement of radiation from the sky or from the room is compared with the calibration data, it must first be multiplied by a factor equal to the ratio of the solid angle of the whole beam to that covered by the calibrator. These factors are determined by comparing the signals in the different spectral responses from the blackbody calibrator at 80°K with those from the room, an excellent blackbody at ~300°K. Both temperatures are in the Rayleigh-Jeans range for all spectral responses. The factors are 0.81, 0.73, 0.68, 0.65, and 0.59, for SR1 through SR5.

4. Flight Train and Description of a Flight

The flight train had the following components in both the June and September flights. At the top is a Raven Industries 11.7 million cubic foot balloon of 0.0007-in. polyethylene, which by itself weighs 1360 lb. Suspended below the balloon by its own parachute is a reel which carries 2000 ft of 3/8-in. nylon line and lowers the scientific payload away from the balloon in flight. A telemetry package including a radiosonde and tracking beacon, as well as the command system for the letdown reel, is mounted on the reel framework. The scientific package hangs by its parachute at the bottom of the 2000-ft nylon line from which it is cut loose by a squib when the flight is terminated. The scientific telemetry is in a separate box which rides on top of the instrument package. Below the package is a crush pad of corrugated cardboard.

The reel increases the probability of failure of the balloon flight and complicates the flight. The reel has been tested for payloads of approximately 500 lb. The scientific package and its telemetry, parachute, and rigging in our flights weigh ~500 lb and therefore leave no margin. The present state of the ballooning art requires, however, that it be possible to decrease the weight of the flight train as the balloon traverses the troposphere where the atmospheric temperature is at a minimum. In this region there is a tendency for balloons to reduce their rate of ascent and, in effect, to get stuck. Although one might think that by increasing the free lift on the ground this could be avoided, there is a constraint on fast ascent rates imposed by the thermal shock on the balloon as it enters the troposphere.

The solution now used is to carry some disposable ballast, typically 10% of the total flight-train weight (200 lb in our case), which is released while the balloon is in the troposphere and the lower stratosphere. In both flights, the ballast was carried in 10 bags mounted on a beam placed just above the reel. These bags are ruptured on command to release the ballast, which is a steel powder of approximately Gaussian distribution with a 0.013-in. diameter mean and 0.004-in. variance. By the time the ballast reaches the payload it is dispersed over a large area; nevertheless, several particles strike each cm^2 of the payload. The outer cover on the radiometer protects the instrument against this shower. In the June flight, however, at least one of the larger ballast particles did manage to pierce the outer cover and, by a sequence of events that will be described, shattered the membrane. For the September flight we sieved the ballast to exclude particles with diameters greater than 0.015 in.

Once ready for flight – batteries charged, telemetry and payload checked out – the apparatus is stored warm and we wait for good weather. We require a prediction (at 11 a.m. or earlier on the flight day) of a reasonable chance of surface and low-level (~500 ft) winds less than 12 knots, less than 10% cirrus cloud cover, no cumulus clouds, and little chance of afternoon thunderstorms. If these conditions are promised, we pump

out the sealed copper can and fill it with helium gas that has been passed through a liquid-nitrogen trap to remove water and oil. Next, we begin the struggle against frost formation. During the nitrogen and helium transfer the storage dewar is clothed in two nested polyethylene bags that isolate the apparatus from room atmosphere. These bags are in addition to those shown in the schematic drawing of the apparatus (Fig. V-1). Dry nitrogen, the efflux from liquid nitrogen, is circulated through the storage dewar for approximately half an hour. Then liquid nitrogen is transferred into the storage dewar until approximately 3-4 liters has accumulated. The transfer is stopped and a heater located at the bottom of the storage dewar is turned on to maintain a positive pressure of dry nitrogen in the bags, as well as to produce a cold gas flow past the copper can and cones. At this point, a second weather briefing is taken to reassess the possibilities for the flignt before we transfer the liquid helium. If the weather still looks favorable, the liquid nitrogen is removed by boiling it out with increased power in the heater. After the nitrogen is exhausted, the storage dewar is flushed with clean helium gas and the liquid-helium transfer begins through the two polyethylene bags. At this point the membrane which makes a gas seal to the inner cone is tightened down. As soon as a liquid-helium level has been established, the seal in the copper can is opened, and the liquid-helium transfer tube is inserted into the copper can. The rest of the filling operation is performed in this configuration until both the copper can and the storage dewar are filled to capacity (~55 liters). The entire transfer requires approximately 85 liters of liquid helium. The transfer tube is removed, the copper can is sealed again, and the holes for the transfer tube in the two polyethylene bags are sealed. After the outer parts of the apparatus have come back to room temperature, the bags are removed and the outer cover is installed. A flow of clean helium gas is maintained in the region between the outer cover and the membrane. Next, the inflight calibrator is installed. A preflight calibration in all filter positions is performed, using the 300°K room radiation. The package is now turned over to the NCAR crew for final rigging on the launch vehicle.

A final checkout is performed in the field; if this is successful and if the weather is still satisfactory, the balloon is inflated (see Fig. V-11).

At launch the dewar is tipped so that the optical axis of the radiometer is 20° from the zenith. The flight train begins to ascend at ~900 ft/min, a rate that is maintained during most of the ascent. At 5000 ft altitude the deployment of the 2000-ft line begins. The entire deployment takes approximately 20 minutes. After deployment of the line, the telemetry transmitter for the reel is turned off and a study of RF interference from the remaining sources begins.

Although the RF immunity studies can begin on the ground, the actual flight configuration of the antennas connot be duplicated. It is easy to determine RF interference caused by the 1.7-mHz beacon, since we can turn it off at will and see if there is an

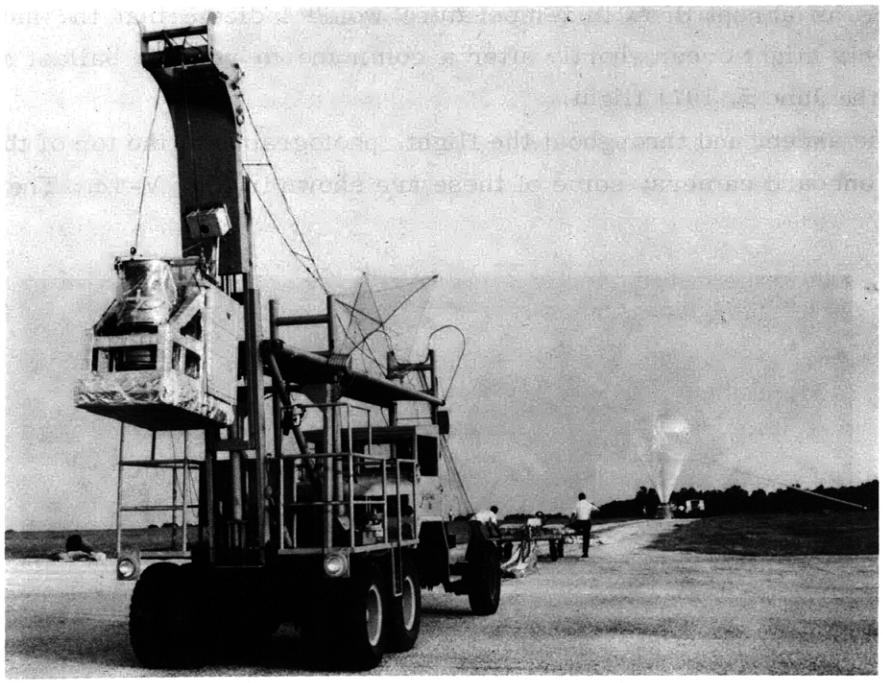

Fig. V-11. Balloon package ready for launching (June 5, 1971).

effect on the radiometer output. Determining the RF interference from the 235-mHz payload telemetry is more difficult, since the telemetry is our only link to the experiment during the flight. One scheme that we use is to send a command that attenuates the transmitted power by one-half and then look for a change in the radiometer output. We do this throughout the flight but especially at float altitude when the radiometer signals are small. This procedure is used only for diagnostic purposes. Throughout the flight we have periods when we turn the telemetry off entirely and rely on the onboard tape recorder so that in case there is RF interference we have some data that are free of radiofrequency.

Although we had considerable difficulty with RF interference in the flight made in September 1969, there was no problem in either of the 1971 flights.

Some of the measures that we took to avoid RF interference are as follows. All leads that communicate between the inside of the electronics compartment and the outside world pass through π section RF filters. The electronics compartment itself has finger stock gaskets on the doors. The leads in the signal circuitry run in double-shielded coaxial cables. Finally, the telemetry antenna hangs below the package by a 30-ft cable. The antenna is a half-wave dipole with a ground plane oriented so that the apparatus is in the antenna's cone of silence.

The various temperatures of the inner cone are monitored continuously during the

ascent, since an abrupt drop in temperature would indicate that the membrane had ruptured. This might occur shortly after a command to release ballast is given, as happened in the June 5, 1971 flight.

During the ascent and throughout the flight, photographs of the top of the dewar are taken by the onboard camera; some of these are shown in Fig. V-12. These pictures

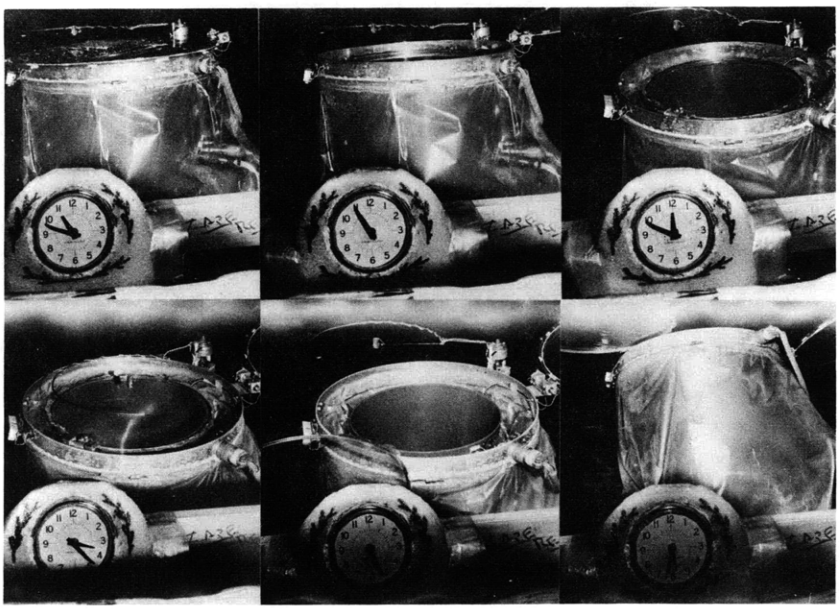

Fig. V-12. Inflight photographs of the apparatus (September 29, 1971).

show such things as the positions of the cover and membrane, the frost accumulation and the operation of the inflight calibrator.

As soon as all ballast has been released, we remove the outer cover. This is verified in flight by a signal from a microswitch actuated by the cover frame and also by a change in the radiometer output voltage. In the September 29, 1971 flight the reduction in radiometer signal when the cover was removed was 1.09×10^{-7} rms detector volts in SR1. This value is within a factor of two of that calculated by using the measured absorption coefficients of mylar and the ambient temperature.

At float altitude we begin a program of zenith scanning that is carried out in two ways. One way is to hold the zenith angle fixed and go through the entire filter sequence quickly, calibrating once in each filter position. The second way is to hold the filter fixed and continuously vary the zenith angle from 1° out to 45° and back again, calibrating at 22° in the return scan. Both of these procedures continue throughout the 8 hours that the instrument is at float altitude.

In the September flight the membrane was removed 3 1/2 h before termination of

the flight, in order to determine the radiative contribution by the membrane and also to carry out the experiment without any radiative source directly in the beam.

We had always considered the removal of the membrane, even at flight altitudes, a risky affair. There are still several mm Hg of air at flight altitude, and it seemed reasonable to suppose that it would not take long before the cold regions of the instrument would become covered with air snow. The snow would be most likely to scatter the incoming radiation, and to affect high-frequency more than low-frequency radiation. We find, however, that nothing happens to the radiometer signals, including the amplitude of the inflight calibration signals, until the liquid helium in the storage dewar has been exhausted. After this, a slowly increasing attenuation which is frequency-dependent does set in.

We inadvertently gained some experience with this phenomenon in the June 5, 1971 flight, in which the membrane was opened for most of the flight. When the instrument was almost at float altitude, a large ballast particle pierced the outer cover and then shattered a thin polyethylene membrane which at the time was at a temperature of 120°K. The chain of events that followed is amusing but only in retrospect. The draft of cold helium gas released by the broken membrane cooled the outer cover enough to shrink it out of its frame. When the command was given to release the cover, the frame moved but the cover remained virtually in place. Eventually, the inflight calibrator pushed the cover aside, and finally the command to release the membrane cleared the entire area at the top of the storage dewar.

The most likely reason why little snow collects in the instrument while there is still helium in the storage dewar is that the helium efflux gas forms a jet in the inner cone when the membrane has been removed. Some independent evidence for this comes from the fact that the inflight calibrator cools down when it is brought into the field of view after the membrane has been removed. In the September 29, 1971 flight the signals contributed by the mylar membrane were 1.45×10^{-8} and $(3\pm1) \times 10^{-9}$ rms V at the detector for SR1 and SR2. These are approximately twice the predicted values.

Both before and after the membrane is removed we attempt to get an estimate of the radiative contributions of the inner cone by changing its temperature. This is accomplished by increasing the flow of helium efflux gas past the cone by turning on a heater in the liquid helium. The temperature of the cone is measured at 4 locations along its length. If there is a change in radiometer signal which correlates with these temperatures, we can estimate the emissivity of the cone, knowing the fraction of the beam that the cone intercepts.

5. Data and Interpretation

The data from the September 29, 1971 flight and its interpretation will now be discussed. Figure V-13 is a plot of the inflight calibration signals for all spectral responses

as a function of time during flight. The calibrations were performed at many different zenith angles. The data in the figure have been normalized to a calibrator temperature of 100°K; the actual temperatures are in the range 250-100°K. The data reveal a 10% change of overall system gain from the beginning to the end of the flight. The points on the right in Fig. V-13 are the calculated calibration signals at a calibrator temperature of 100°K. These calculations are based on the measured response of the radiometer to a Rayleigh-Jeans source and the fraction of the radiometer beam covered by the calibrator in each spectral response. The calibrator covers 1.47, 1.18, 0.96, 0.93, 0.81×10^{-2} of the total beam in SR1 through SR5.

Figure V-14 shows the zenith-angle dependence of the signals in the various spectral responses after the membrane had been removed. The data presented are averages for 2 zenith scan sequences and 9 rapid filter sequences at fixed zenith angles. Three corrections have been applied to the original data. First, the offset measured in the blocked position of the filter disk is subtracted from each point. In the rapid filter sequences, the offset measured in the sequence is subtracted from the other points in that sequence. In the scan sequence, the offset scan measured in the blocked position is subtracted from all other scans in the sequence. The offset fluctuates throughout the flight; it is typically a few nanovolts referred to the detector. Second, the averaged signals have been multiplied by the ratio of the solid angle subtended by the primary laboratory calibrator to the solid angle subtended by the entire radiometer beam in each spectral response. Finally, the signals have been adjusted to a radiometer temperature of 0°K. The last two corrections facilitate the comparison of the unknown signals with the calibrations.

The zenith scanning data for SR1 and SR2 show two significant features. The increase in signal at small zenith angles is caused by the reflection of radiation from the Earth and the lower atmosphere by the 0.0018-cm thick polyethylene balloon. Emission of radiation by the balloon is small in comparison. The balloon subtends 6° at the radiometer. When near the center of the radiometer's field of view it contributes signals of 160, 17, 5.5, and 5.2 nV in SR1, SR2, SR3, and SR4. The balloon contribution is calculable at all angles but becomes negligible relative to the observed signals for zenith angles greater than 20°.

The second feature in the zenith scanning data of SR1 and SR2 is the slow increase in signal with angle for large zenith angles. We attribute this to the atmosphere; it is a larger effect in SR1, which includes more atmospheric emission lines, than in SR2. The signal-to-noise ratio in SR3, SR4, and SR5 is not good enough to determine a zenith-angle dependence.

Unfortunately, the actual atmospheric contribution to the total radiometer signal is not determined uniquely by the variation of the signal with zenith angle. A detailed model for the atmospheric radiation is required. The only model-independent calculation

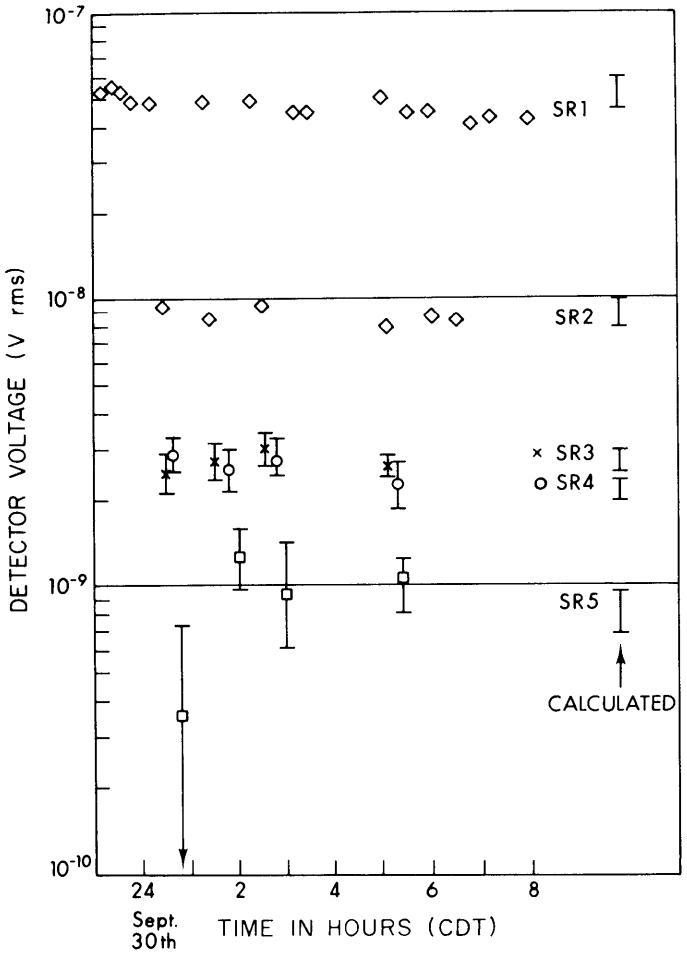

Fig. V-13.
Inflight calibration signals vs time (September 30, 1971).

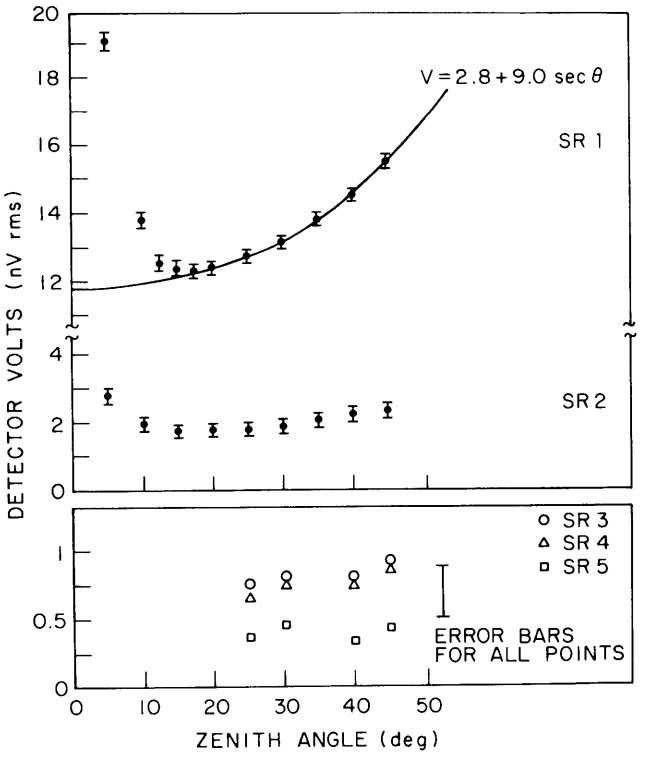

Fig. V-14.
Radiometer signal vs zenith angle (September 29, 1971).

that can be made directly from the data is an estimate for the lower limit of the atmospheric contribution.

If the temperature and composition of the atmosphere are only functions of altitude, sec θ gives the strongest possible dependence of the atmospheric radiation on zenith angle. The limiting case of sec θ occurs when the radiation sources are at low enough altitudes that the curvature of the atmosphere can be neglected, and also if the atmospheric emission lines are unsaturated. This means that the spectral brightness at the emission-line center is much less than the spectral brightness of a blackbody at the temperature of the atmosphere. For other cases the atmospheric radiation varies more slowly with zenith angle. For saturated lines the total power radiated depends on the line shape. The total radiation from saturated but narrow pressure-broadened lines with a Lorentzian shape varies as the square root of the number of molecules along the observation path. This corresponds to a $\sec^{1/2}\theta$ zenith-angle dependence. Radiation by saturated Doppler-broadened lines would vary still more slowly with zenith angle.

The total voltage across the detector as a function of angle is given by

$$V_T(\theta) = V_{iso} + V_{atm}(0)\, f(\theta).$$

V_T is the total signal voltage at any zenith angle, V_{iso} is the voltage arising from the isotropic component, $V_{atm}(0)$ is the atmospheric contribution at the zenith, and $f(0)$ is the atmospheric zenith-angle dependence. If we fit the scanning data to the limiting case for which $f(\theta)$ is sec θ, V_{iso} and V_{atm} are 2.8 ± 0.6 and 9 ± 0.6 nV in SR1, and 0.25 ± 0.7 and 1.5 ± 0.7 nV in SR2. The data cannot be fitted with $\sec^{1/2}\theta$ for the atmospheric dependence in either SR1 or SR2 because this would make the atmospheric contribution to the signal greater than the total measured signal.

The known atmospheric constituents which have emission lines in the region between 1 cm^{-1} and 30 cm^{-1} are O_3, H_2O, O_2, N_2O, CO and OH. Of these ozone, water, and oxygen make the greatest contribution to the atmospheric radiation at flight altitude.

Figure V-15 shows the integrated spectral brightness calculated for each atmospheric constituent at 38.5-km altitude, where the atmospheric pressure is 2.5 mm Hg. The assumptions made for each constituent will be discussed. The theory for the atmospheric calculations is described in the appendix.

The ozone lines result from transitions between rotational levels of the asymmetric rotor. The frequencies and strengths of these lines have been tabulated by Gora[22] and by Clough.[23] The lines are weak but numerous; they almost form a continuum. The estimated radiation is based on an average atmospheric temperature of 250°K and on the ozone concentrations given in the U.S. Standard Atmosphere Supplements.[24] The assumed column density of ozone is 3×10^{17} molecules/cm^2. There is, however, a substantial uncertainty in this number.[25] The ozone lines are unsaturated.

Radiation by water is also due to transitions between rotational levels. Water is an

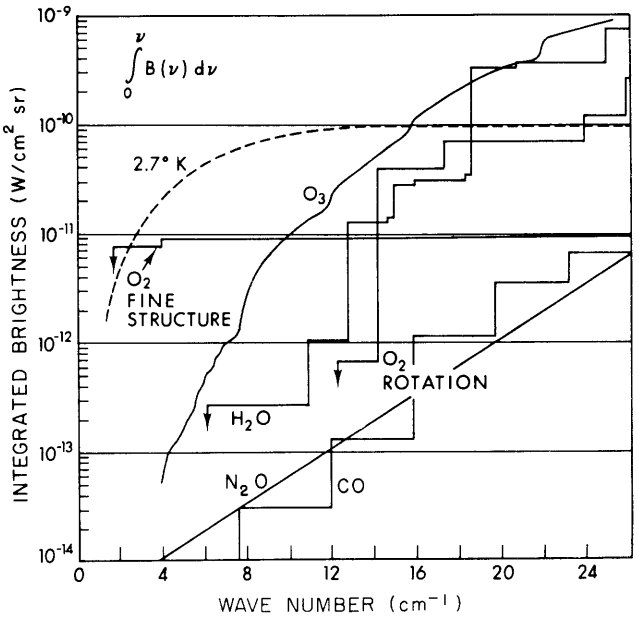

Fig. V-15. Calculated radiation from atmospheric constituents at 39 km.

asymmetric rotor with a complex spectrum. The water-line frequencies, strengths, and widths have been tabulated by Benedict and Kaplan.[26] The column density of water is uncertain. Over the years, measurements of the mixing ratio of water to air in the stratosphere have varied[27] by a factor of 100. Recent measurements by Murcray et al.[28] at 30 km give mixing ratios between 2 and 3×10^{-6} gm/gm. Gay[29] has measured mixing ratios of the order of 4×10^{-7} gm/gm. We have assumed a column density for water of 3×10^{17} molecules/cm^2, which corresponds to a mixing ratio of 2.5×10^{-6} gm/gm. The strong water lines are fully saturated.

The radiation by oxygen molecules can be calculated with some confidence, since the density as a function of altitude is known. The oxygen radiation lines in the far infrared region come from two different transition mechanisms in the molecule. At low frequencies there is a cluster of lines near 2 cm^{-1} and a single line at 4 cm^{-1}. These lines come from magnetic dipole transitions between states within one rotational level but with different relative orientations of the rotational and electronic spin angular momentum. They have been tabulated by Meeks and Lilley.[30] There is also a set of lines above 12 cm^{-1} that are attributable to magnetic dipole transitions between different rotational states of the molecule. The rotational spectrum has been tabulated by Gebbie, Burroughs, and Bird.[31] The column density of oxygen is 1.4×10^{22} molecules/cm^2. The lines are not completely saturated.

Radiation by N_2O and CO arises from the simple rotational spectrum of a linear molecule in the ground vibrational state. The emission lines and strengths are calculated

by standard methods using published molecular constants.[32] The column densities are not well known. Seeley and Houghton[33] have established an upper limit of 10^{-7} gm/gm for the mixing ratio of both species above 10 km altitude. It is believed that these molecules are generated at the surface of the Earth, so that their mixing ratios are unlikely to increase with altitude. Assuming a constant mixing ratio at all altitudes above 10 km sets an upper limit for the column density above 39 km. The resulting column density is 10^{16} molecules/cm^2 for both N_2O and CO.

The estimated OH concentration in the atmosphere, given by Barrett[34] and Leovy,[35] is of the order of 10^{12} molecules/cm^2. The radiation that falls into our region arises from λ doubling transitions in rotation states with N = 4 or larger. The line intensities are almost independent of frequency, and a calculation using the estimated concentration gives the miniscule brightness of $\sim 5 \times 10^{-20}$ W/cm^2-sr for any line in our region.

Table V-1. Calculated values of the atmospheric contributions in five spectral responses at 39 km altitude. The voltages are in nV rms at the detector.

Constituent	Column Density	SR1	SR2	SR3	SR4	SR5
O_3	3×10^{17}	4	0.36	0.034	0.02	0.0015
H_2O	3×10^{17}	2.8	0.11	0.002	0.002	—
O_2	1.4×10^{22}	0.97	0.12	0.06	0.06	0.06
N_2O	10^{16}	Less than 1% of Total Atmosphere				
CO	10^{16}	Less than 1% of Total Atmosphere				
Total Atmosphere		7.8	0.6	0.1	0.08	0.06
2.7°K Blackbody		1.3	1.0	0.7	0.7	0.4

Table V-1 gives calculated estimates of the atmospheric contributions in each of the spectral responses at an atmospheric pressure of 2.5 mm Hg. The first column lists the assumed conditions. The last row shows the signal that would be expected from a 2.7°K blackbody in each spectral response.

In principle, if ozone and water are the major contributors of atmospheric radiation, it is possible to couple the calculations of the lines in each spectral response with the scanning data. If we assume that the ozone radiation varies with zenith angle as sec θ,

and the water radiation as $\sec^{1/2}\theta$, this would determine separately the column densities of the two constituents, which are the most uncertain quantities. With this information the actual atmospheric contributions to the observed signals, rather than just lower limits, could be established. Unfortunately, the signal-to-noise ratio in SR2 is not good enough to accomplish this. For a future flight we shall make filters for the region between 12 cm^{-1} and 20 cm^{-1} which are better suited for these atmospheric measurements.

A further piece of evidence that the atmosphere makes a substantial contribution to the signal at float altitude in SR1 is provided by the variation in signal with altitude in the September flight. During the ascent, the optic axis of the instrument was maintained at 20° to the zenith. The outer cover was removed at a pressure of 4.7 mm Hg. After the removal of the cover the balloon continued to rise until it reached an atmospheric pressure of 2.2 mm Hg, where it remained for a brief period before settling at a pressure of ~2.5 mm Hg.

The radiometer signal followed these variations in altitude. Figure V-16 shows the pressure at the instrument as a function of time, and Fig. V-17 shows the variation in radiometer signal for SR1 during the ascent. The data in Fig. V-17 have been corrected for dependence of detector responsivity on liquid-helium temperature. The measured radiative contributions of the outer cover and membrane have been subtracted.

The data clearly show that the atmosphere still makes a contribution to the total signal at 2.5 mm Hg, since the curve of signal vs pressure did not flatten out as the instrument approached flight altitude. Figure V-17 shows calculated values of ozone, water, and oxygen radiation in SR1 as a function of pressure. In the ozone calculation the distribution of ozone in the U.S. Standard Atmosphere Supplements[24] is assumed, and this distribution has large fluctuations about the average values given there. Since the ozone lines are unsaturated, the ozone radiation varies directly as the column density above the apparatus. Figure V-17 shows that the signal vs pressure curve could be fitted nicely by just twice as much ozone as has been assumed for this calculation.

Water has been plotted on the basis of a constant mixing ratio of 2×10^{-6} gm/gm and complete saturation of the lines. The oxygen lines are fully saturated for pressures greater than ~3 mm Hg. At pressures lower than this the lines come out of saturation and the slope of oxygen radiation vs pressure doubles.

In conclusion, although no precise estimates of the atmospheric radiation can be made from these data, they indicate that the atmosphere is still very influential at 2.5 mm Hg, and, furthermore, ozone is probably the dominant radiator in the region between 4 cm^{-1} and 20 cm^{-1} for 20-40 km altitudes.

At pressures greater than 80 mm Hg or altitudes less than 15 km, the region from the troposphere down to the ground, the radiation is dominated by water with large

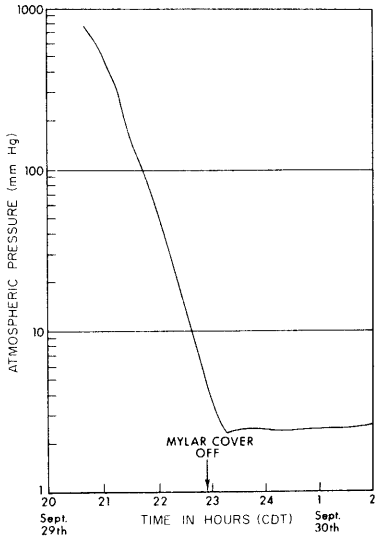

Fig. V-16.

Atmospheric pressure at the radiometer during ascent (September 29-30, 1971).

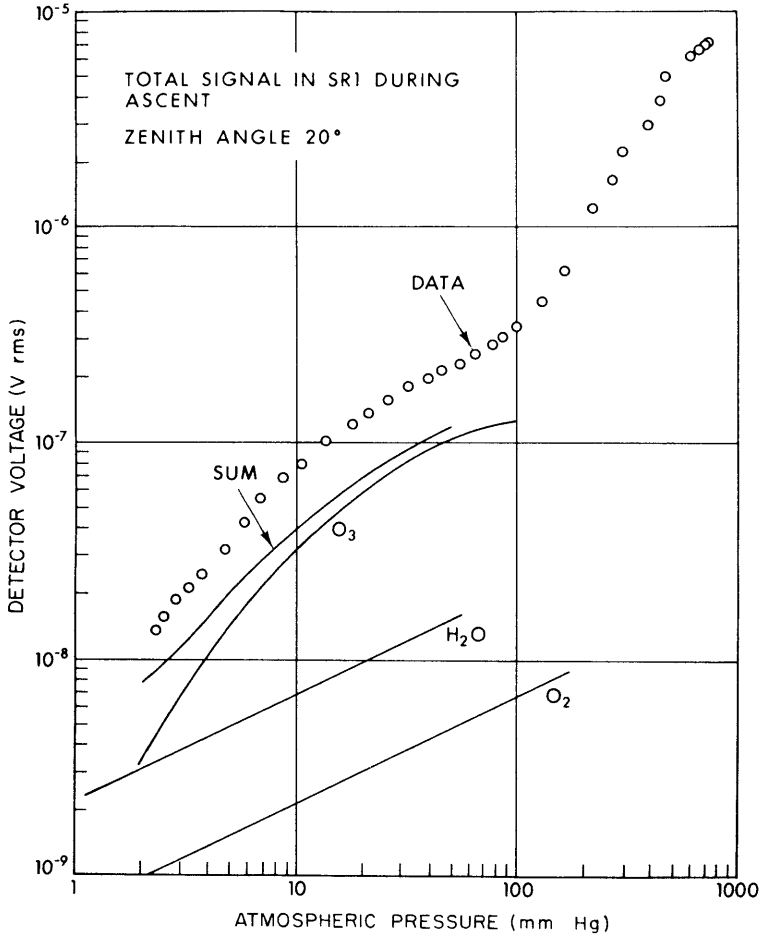

Fig. V-17.

Radiometer signal in SR1 vs pressure during ascent (September 29, 1971).

fluctuations in concentration.

The results of the June flight are listed in Table V-2. Because of difficulties with the cover and the membrane, the useful data in this flight were obtained during the hour remaining between the time the command to remove the membrane was given and the termination of the flight. We did not scan to large zenith angles during this time. The data obtained earlier in the flight suffered uncertain effects because pieces of the membrane and part of the cover remained in the field of view of the radiometer. For these reasons, the atmospheric contribution was not measured in the flight. The atmospheric corrections in Table V-2 are the calculated estimates given in Table V-1. The corrections for the cone are calculated by using the measured cone temperatures, the fraction of the beam intercepted by the cone, and the calculated emissivity. An important result of the June flight is that the data do not show the large spectral brightness between 10 cm^{-1} and 12 cm^{-1} which we had found in our 1969 flight.[14] The spectral responses SR2, SR3, and SR4 were specifically designed to give spectral resolution around this region.

The results of the September 1971 flight are listed in Table V-3. The atmospheric contributions for SR1 and SR2 are the measured lower limits, under the assumption of a sec θ dependence for the atmospheric radiation. The atmospheric contributions for SR3, SR4, and SR5 are the calculated estimates given in Table V-1. The cone contribution is calculated as for the June 5, 1971 flight.

Figure V-18 summarizes all known measurements of the background radiation in the far infrared. Direct balloon and rocket observations, as well as indirect measurements based on absorption spectra of interstellar molecules, are included.

The central panel shows results obtained from optical absorption spectra of interstellar gas clouds including CN, CH, and CH^+ by Bortolot, Shulman, and Thaddeus.[9] From the distribution of rotation states in these molecules they establish the point at 3.8 cm^{-1}, and upper limits at 7.6, 18, and 28 cm^{-1}. Hegyi, Traub, and Carleton[36] have seen the R(2) line of CN; they quote a temperature between 3.6°K and 2.0°K at 7.6 cm^{-1}.

Flux measurements made by broadband radiometers cannot be represented unambiguously in diagrams such as Fig. V-18, since they give weighted frequency integrals of the spectral brightness. For the rocket measurements of Shivanandan, Houck, and Harwit[10] and of Pipher, Houck, Jones, and Hawrit,[12] the spectral brightness shown is found by dividing the total quoted flux by the quoted bandwidth. We present the results of our balloon experiments and the rocket measurement of Blair et al.[13] using the following procedure. First, we establish for each spectral response an equivalent square box response, in the manner described in this report. Next, we assume that the signal observed in a spectral response is entirely due to radiation at frequencies within the equivalent box response. In this way a certain amount of flux is assigned to each

Table V-2. Results of the flight of June 5, 1971.

	SR1	SR2	SR3	SR4	SR5
Total signal at $\theta_z = 25°$ (nV)	15.4 ±1	$1.5^{+.5}_{-.2}$	0.6 ±.3	0.7 ±.3	0.35 ±.2
Equivalent blackbody temperature (°K)	5.6 ±.1	$3.05^{+.25}_{-.15}$	2.6 ±.4	2.7 ±.4	$2.5^{+.5}_{-.7}$
Minimum total flux (10^{-10} W cm^{-2} sr^{-1})	10.3 ±.7	$1.05^{+.4}_{-.2}$	0.43 ±.2	0.55 ±.3	0.3 ±.2
Calculated atmospheric correction (nV)	7.8	0.6	0.1	0.08	0.06
Calculated cone correction (nV)	0.2	0.08	0.025	0.03	0.02
Background signal[a] (nV)	7.4 ±1	$0.8^{+.5}_{-.2}$	0.5 ±.3	0.6 ±.3	0.3 ±.2
Equivalent blackbody temperature (°K)	$4.3^{+.2}_{-.2}$	$2.6^{+.3}_{-.2}$	$2.5^{+.3}_{-.4}$	2.6 ±.4	$2.5^{+.4}_{-.7}$
Minimum corrected flux (10^{-10} W cm^{-2} sr^{-1})	4.9 ±.7	$0.56^{+.4}_{-.2}$	0.36 ±.2	0.49 ±.3	0.25 ±.2
Normalized box spectral response bandwidth (cm^{-1})	1-18.5	1-11.1	1-7.9	1-7.8	1-5.4

[a]Errors do not include uncertainty in calculated corrections.

Table V-3. Results of the flight of September 29, 1971.

	SR1	SR2	SR3	SR4	SR5
Total signal at $\theta_z = 25°$ (nV)	12.4 ±.2	1.7 ±.15	.89 ±.15	.85 ±.15	.47 ±.17
Equivalent blackbody temperature (°K)	5.2 ±.15	3.2 ±.1	2.9 ±.2	2.9 ±.2	2.8 ±.5
Minimum total flux (10^{-10} W cm^{-2} sr^{-1})	8.2 ±.14	1.2 ±.1	.65 ±.15	.68 ±.15	.39 ±.17
Atmospheric correction at $\theta_z = 25°$ assuming sec θ dependence (nV)	≥9	≥0.9	—	—	—
Calculated atmospheric correction (nV)	—	—	0.1	0.08	0.06
Calculated cone correction (nV)	0.2	0.08	0.025	0.03	0.02
Background signal[a] (nV)	≤3.2 ±.2	≤.72 ±.15	.77 ±.15	.74 ±.15	.39 ±.17
Equivalent blackbody temperature (°K)	≤3.4	≤2.7	2.8 ±.2	2.8 ±.2	$2.7^{+.4}_{-.6}$
Minimum corrected flux (10^{-10} W cm^{-2} sr^{-1})	≤2.3	≤0.62	0.56 ±.15	0.60 ±.15	0.33 ±.17
Normalized box spectral response bandwidth (cm^{-1})	1-18.5	1-11.1	1-7.9	1-7.8	1-5.4

[a]Errors do not include uncertainty in calculated corrections.

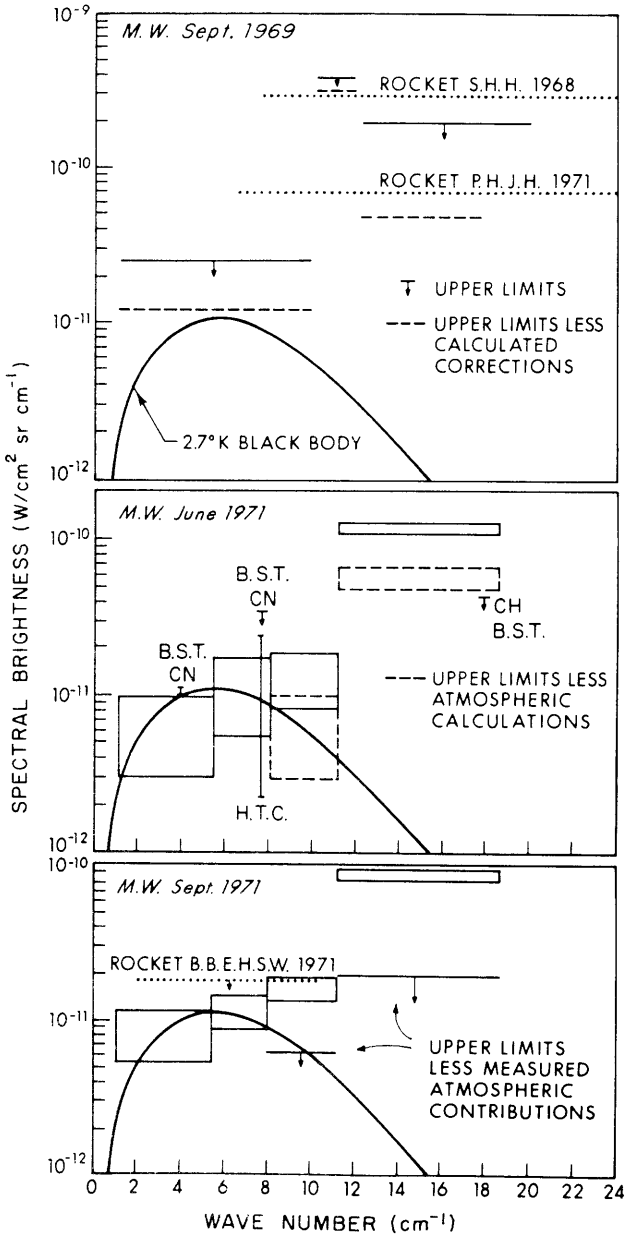

Fig. V-18. Summary of far infrared background measurements.

spectral region between cutoff frequencies of the idealized responses. This difference between the fluxes is plotted as uniformly distributed in that region. The difference between SR3 and SR4 in the 1971 flights is not shown in Fig. V-18. The vertical dimensions of the boxes represent the uncertainties that are due to noise in the observed signals; there is no good way of representing the uncertainty in the entire procedure. This method gives the best results for a smooth source spectrum; for example, a 2.7°K blackbody spectrum looks quite reasonable when transformed in this manner.

The upper panel of Fig. V-18 shows the results of the rocket measurements of Shivanandan, Houck, and Harwit, and of Pipher, Houck, Jones, and Harwit, and also those of our first balloon flight, in September 1969. For the balloon flight we plot both the total spectral brightness and corrected values based on estimates of the effects of the atmosphere and "hot" parts of the instrument near the radiometer beam.

The middle panel shows both total and corrected values of the spectral density in the June 1971 balloon flight. The corrections are based on calculations of the atmospheric radiation.

The lower panel displays the results of the September 1971 flight. The total spectral brightness, as well as the upper limits for the isotropic background, are plotted. These upper limits are based on the minimum values for the atmospheric contribution as determined from the zenith scanning data.

Figure V-19 shows the region of the sky which was observed in the September 1971

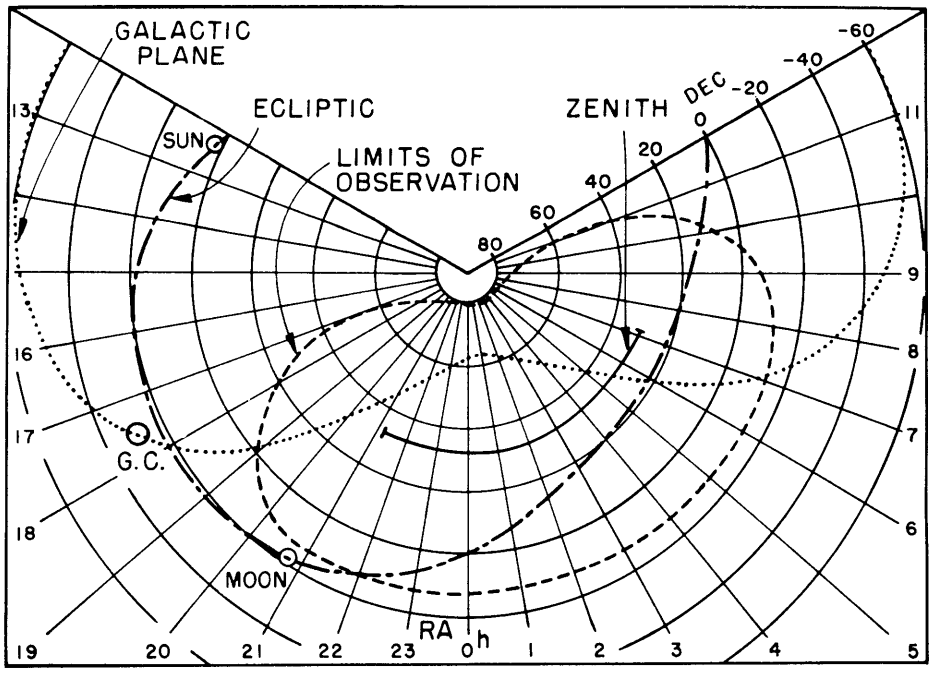

Fig. V-19. Region of sky observed (September 29, 1971).

flight, in equatorial coordinates. The zenith during the time the balloon was at float altitude is indicated, as well as the region of the sky within 45° of the zenith. The radiometer beam swept much of this area as it scanned through zenith angle and azimuth. The azimuth scanning resulted from torsional oscillation of varying amplitude performed by the instrument package at the end of the 2000-ft line which connected it to the balloon. The average heading about which the package oscillated changed slowly throughout the flight. The equilibrium position of the package was probably fixed by a local wind at the package. The balloon and package both traveled through the atmosphere at the velocity of the wind at the balloon altitude. At the package, 2000 ft below the balloon, the wind velocity may have differed by as much as 10 m/s, so that the package was in a substantial local wind. It is worth noting that such a wind would have carried away local "air pollution" generated by the package.

We cannot set good limits on the isotropy of that part of the signal which can be attributed to background radiation. The signal in SR1 was isotropic to 20% or better; that in SR2 to 40%. For the other spectral responses we can say only that there was no evident dependence of the signal on the part of the sky that was being observed.

6. Conclusions and Discussion

The uncorrected radiometer signal sets upper limits on the background radiation flux. The flux in SR3, SR4, and SR5 is close to that expected from a 2.7°K blackbody, while in SR1 and SR2 the flux is larger. The uncorrected flux in SR1 is smaller than, but comparable to, that measured in a similar bandwidth in the rocket experiment of Pipher, Jones, Houck, and Harwit.[12] The uncorrected flux in SR2 and SR3 indicates, as Blair et al.[13] also have discovered, that there does not appear to be a strong "line" between 10 cm^{-1} and 12 cm^{-1}, as the results of our first balloon flight in 1969 had implied.

We believe that a substantial part of the flux observed in SR1 and SR2 is due to the atmosphere, and cannot rule out the possibility that all of the flux above ~10 cm^{-1} is of atmospheric origin. This conclusion is based on the following points. (i) The calculated atmospheric radiation is of the same order of magnitude as the observed flux; but we cannot make a precise calculation of the atmospheric contribution because the column densities of ozone and water are uncertain. (ii) The steep slope of the signal vs pressure curve at flight altitude also suggests a large atmospheric contribution; however, this observation cannot be made quantitative without detailed knowledge of the distribution of the atmospheric constituents. (iii) The increase in signal with increasing zenith angle yields a model-independent estimate of the minimum atmospheric contribution. We have used this estimate to correct the raw flux in SR1 and SR2.

If our interpretation of the excess flux is correct, the measured background spectrum is consistent with a 2.7°K thermal distribution. Our corrected minimum

background flux for SR1 of $\leq 2.3 \times 10^{-10}$ W/cm^2 sr is in substantial disagreement with the minimum flux of 1.3×10^{-9} W/cm^2 sr quoted by Pipher, Jones, Houck, and Harwit. We have found no explanation for this discrepancy. Harwit[37] has suggested that the increase in signal with zenith angle in our experiment may be due to earthshine, radiation from the earth and lower atmosphere, which scatters into the radiometer. This seems to us unlikely, but we cannot rule it out entirely because we have not been able to measure the radiometer beam profile at very large angles.

In a future flight we shall make measurements with increased spectral resolution in the 12-20 cm^{-1} region, with particular emphasis on filters that can separate the ozone and water contributions. We also plan to place another baffle around the radiometer dewar to test the earthshine hypothesis.

We are indebted to Richard L. Benford for his technical assistance in all phases of the experiment, and thankful for the support offered and interest in this experiment shown by Professor A. G. Hill and Professor B. F. Burke. Dr. Nancy Boggess of the Office of Space Science and Applications of NASA has been extremely helpful in our effort to carry out this experiment. The staff of the National Center for Atmospheric Research, in Palestine, Texas, is a joy to work with and the success of these experiments is a tribute to their skill.

Appendix

The line strength is given by

$$S = \frac{8\pi^3 \nu}{3hc}\left(\frac{N_i}{g_i} - \frac{N_j}{g_j}\right)|\mu_{ij}|^2,$$

where ν is the frequency, h Planck's constant, c the velocity of light, N_i the number of molecules/cm^2 in the upper state, and g_i the multiplicity. N_j and g_j are for the lower state, μ_{ij} is the matrix element coupling the two states, and S is in units of sec^{-1}. If kT is large compared with $h\nu$, the population difference in the two states is approximated by

$$\frac{N_i}{g_i} - \frac{N_j}{g_j} = \frac{h\nu}{kT} Nf,$$

where f is the partition sum fraction in the upper state. If the energy levels involved are rotational states of molecules with $hB/kT \ll 1$, where B is the rotation constant, the partition sum fraction is given by

$$f \approx (2J+1)\frac{hB}{kT}\exp(-hBJ(J+1)/kT).$$

The line strength becomes

$$S = \frac{8\pi^3 \nu^2 hB}{3c(kT)^2} (2J+1) \exp(-hBJ(J+1)/kT) \left|\mu_{ij}\right|^2 N.$$

The total absorption coefficient at frequency ν is related to the line strength of a Lorentzian line of width $\Delta\nu_L$ by

$$\gamma_\nu = \frac{S}{\pi} \frac{\Delta\nu_L}{(\nu-\nu_o)^2 + (\Delta\nu_L)^2}.$$

The integrated fractional absorption by the line is given by

$$A = \int_0^\infty \left(1 - e^{-\gamma_\nu}\right) d\nu.$$

As is well known, this integral is

$$A = 2\pi\Delta\nu_L x e^{-x} \left[J_o(ix) - iJ_1(ix)\right],$$

where J_o and J_1 are Bessel functions of the first kind, and x is defined by $S/2\pi\Delta\nu_L$.

If $x \ll 1$, the line is unsaturated and $A = S$. If $x \gg 1$, the line is fully saturated and $A = 2(S\Delta\nu_L)^{1/2}$. The linewidth in most cases is the collision width.

By Kirchhoff's law, the radiation in a line from a source at temperature T is given by

$$I(\nu) = B_{bb}(\nu, T)A.$$

$I(\nu)$ is the radiation from the line in W/cm^2 sr. $B_{bb}(\nu, T)$ is the spectral brightness of a blackbody at temperature T and frequency ν per unit frequency interval.

D. J. Muehlner, R. Weiss

References

1. A. A. Penzias and R. W. Wilson, Astrophys. J. 142, 419 (1965).
2. R. H. Dicke, P. J. E. Peebles, P. G. Roll, and D. T. Wilkinson, Astrophys. J. 142, 414 (1965).
3. G. Gamow, in A. Beers (Ed.), Vistas in Astronomy, Vol. 2 (Pergamon Press, New York, 1956), p. 1726.
4. A. M. Wolfe and G. R. Burbidge, Astrophys. J. 156, 345 (1969).
5. P. E. Boynton, R. A. Stokes, and D. T. Wilkinson, Phys. Rev. Letters 21, 462 (1968).

6. R. B. Partridge and D. T. Wilkinson, Phys. Rev. Letters 18, 557 (1967).

7. E. K. Conklin and R. N. Bracewell, Nature 216, 777 (1967).

8. G. B. Field and J. L. Hitchcock, Phys. Rev. Letters 16, 817 (1966).

9. V. I. Bortolot, Shulman, and P. Thaddeus (submitted for publication).

10. K. Shivanandan, J. R. Houck, and M. O. Harwit, Phys. Rev. Letters 21, 1460 (1968).

11. J. R. Houck and M. Harwit, Astrophys. J. 157, L45 (1969).

12. J. L. Pipher, J. R. Houck, B. W. Jones, and M. Harwit, Nature 231, 375 (1971).

13. A. G. Blair, J. G. Beery, F. Edeskuty, R. D. Hiebert, J. P. Shipley, and K. D. Williamson, Jr., Phys. Rev. Letters 27, 1154 (1971).

14. D. Muehlner and R. Weiss, Phys. Rev. Letters 24, 742 (1970).

15. D. E. Williamson, J. Opt. Soc. Am. 42, 712 (1952).

16. W. Witte, Infrared Phys. 5, 179 (1965).

17. R. Ulrich, Infrared Phys. 7, 65 (1967).

18. D. Muehlner and R. Weiss, Quarterly Progress Report No. 100, Research Laboratory of Electronics, M.I.T., January 15, 1971, p. 52.

19. B. V. Rollin, Proc. Phys. Soc. (London) 76, 802 (1960).

20. A. Arnaud and G. Quentin, Phys. Letters 32A, 16 (1970).

21. R. W. Keyes, Phys. Rev. 99, 490 (1955).

22. E. K. Gora, J. Mol. Spectry. 3, 78 (1959).

23. S. A. Clough, Air Force Cambridge Research Laboratory, Private communication, 1970.

24. U.S. Standard Atmosphere Supplements, 1966 (U.S. Government Printing Office, Washington, D.C., 1967).

25. B. J. Conrath, R. A. Hanel, V. G. Kunde, and C. Prabhakara, J. Geophys. Res. 75, 5831 (1970).

26. W. S. Benedict, University of Maryland, Private communication, 1969.

27. H. J. Mastenbrook, J. Atmospheric Sci. 25, 299 (1968).

28. D. G. Murcray, T. G. Kyle, and W. J. Williams, J. Geophys. Res. 74, 5369 (1969).

29. J. Gay, Astron. Astrophys. 6, 327 (1970).

30. M. L. Meeks and A. E. Lilley, J. Geophys. Res. 68, 1683 (1963).

31. H. A. Gebbie, W. J. Burroughs, and G. R. Bird, Proc. Roy. Soc. (London) A 310, 579 (1969).

32. See C. H. Townes and A. L. Schawlow, Microwave Spectroscopy (McGraw-Hill Book Company, Inc., New York, 1955).

33. J. S. Seeley and J. T. Houghton, Infrared Phys. 1, 116 (1961).

34. A. H. Barrett, Private communication, 1971.

35. C. B. Leovy, J. Geophys. Res. 74, 417, (1969).

36. D. J. Hegyi, W. A. Traub, and N. P. Carleton (submitted for publication).

37. M. Harwit, Cornell University, Private Communication, 1972.

B. ELECTROMAGNETICALLY COUPLED BROADBAND GRAVITATIONAL ANTENNA

1. Introduction

The prediction of gravitational radiation that travels at the speed of light has been an essential part of every gravitational theory since the discovery of special relativity. In 1918, Einstein,[1] using a weak-field approximation in his very successful geometrical theory of gravity (the general theory of relativity), indicated the form that gravitational waves would take in this theory and demonstrated that systems with time-variant mass quadrupole moments would lose energy by gravitational radiation. It was evident to Einstein that since gravitational radiation is extremely weak, the most likely measurable radiation would come from astronomical sources. For many years the subject of gravitational radiation remained the province of a few dedicated theorists; however, the recent discovery of the pulsars and the pioneering and controversial experiments of Weber[2, 3] at the University of Maryland have engendered a new interest in the field.

Weber has reported coincident excitations in two gravitational antennas separated 1000 km. These antennas are high-Q resonant bars tuned to 1.6 kHz. He attributes these excitations to pulses of gravitational radiation emitted by broadband sources concentrated near the center of our galaxy. If Weber's interpretation of these events is correct, there is an enormous flux of gravitational radiation incident on the Earth.

Several research groups throughout the world are attempting to confirm these results with resonant structure gravitational antennas similar to those of Weber. A broadband antenna of the type proposed in this report would give independent confirmation of the existence of these events, as well as furnish new information about the pulse shapes.

The discovery of the pulsars may have uncovered sources of gravitational radiation which have extremely well-known frequencies and angular positions. The fastest known pulsar is NP 0532, in the Crab Nebula, which rotates at 30.2 Hz. The gravitational flux incident on the Earth from NP 0532 at multiples of 30.2 Hz can be 10^{-6} erg/cm^2/s at most. This is much smaller than the intensity of the events measured by Weber. The detection of pulsar signals, however, can be benefited by use of correlation techniques and long integration times.

The proposed antenna design can serve as a pulsar antenna and offers some distinct advantages over high-Q acoustically coupled structures.

2. Description of a Gravitational Wave in the General Theory of Relativity

In his paper on gravitational waves (1918), Einstein showed by a perturbation argument that a weak gravitational plane wave has an irreducible metric tensor in an

almost Euclidean space. The total metric tensor is $g_{ij} = \eta_{ij} + h_{ij}$, where

$$\eta_{ij} = \begin{pmatrix} 1 & & & \\ & -1 & & \\ & & -1 & \\ & & & -1 \end{pmatrix}$$

is the Minkowski background metric tensor, h_{ij} is the perturbation metric tensor resulting from the gravitational wave, and it is assumed that all components of this tensor are much smaller than 1. If the plane wave propagates in the x_1 direction, it is always possible to find a coordinate system in which h_{ij} takes the irreducible form

$$h_{ij} = \begin{pmatrix} 0 & \cdots & 0 \\ \cdots & \cdots & \cdots \\ 0 & \cdots & \begin{matrix} h_{22} & h_{23} \\ h_{32} & h_{33} \end{matrix} \end{pmatrix}$$

with $h_{22} = -h_{33}$, and $h_{23} = h_{32}$. The tensor components have the usual functional dependence $f(x_1 - ct)$.

To gain some insight into the meaning of a plane gravitational wave, assume that the wave is in the single polarization state $h_{23} = h_{32} = 0$, and furthermore let $h_{22} = -h_{33} = h \sin(kx_1 - \omega t)$. The interval between two neighboring events is then given by

$$ds^2 = g_{ij}dx^i dx^j = c^2dt^2 - \left[dx_1^2 + (1 + h\sin(kx_1 - \omega t))\, dx_2^2 + (1 - h\sin(kx_1 - \omega t))\, dx_3^2\right].$$

The metric relates coordinate distances to proper lengths. In this metric coordinate time is proper time; however, the spatial coordinates are not proper lengths. Some reality can be given to the coordinates by placing free noninteracting masses at various points in space which then label the coordinates. The proper distance between two coordinate points may then be defined by the travel time of light between the masses. Assume a light source at $x_2 = -a/2$ and a receiver at $x_2 = a/2$. For light, the total interval is always zero so that

$$ds^2 = 0 = c^2dt^2 - (1 + h\sin(kx_1 - \omega t))\, dx_2^2.$$

Since $h \ll 1$,

$$cdt = \left[1 + \frac{h}{2}\sin(kx_1 - \omega t)\right] dx_2.$$

If the travel time of light, Δt, is much less than the period of the wave, the integral for

Δt becomes simple and we get

$$\Delta t = \left(1 - \frac{h}{2} \sin \omega t\right) \frac{a}{c}.$$

In the absence of the gravitational wave $\Delta t = \ell_o/c = a/c$, the coordinate distance becomes the proper length. The variation in Δt because of the gravitational wave is given by

$$\delta \Delta t = \left(\frac{h}{2} \sin \omega t\right) \frac{\ell_o}{c}.$$

This can be interpreted as though the gravitational wave produces a strain in space in the x_2 direction of

$$\frac{\Delta \ell}{\ell_o} = \frac{h}{2} \sin \omega T = \frac{h_{22}}{2}.$$

There is a comparable strain in the x_3 direction, however, inverted in phase.

This geometric description of the effects of a gravitational wave is useful for showing the interaction of the wave with free stationary particles. It becomes cumbersome when the particles have coordinate velocities or interact with each other. Weber[4] has developed a dynamic description of the effect of a gravitational wave on interacting matter which has negligible velocity. For the case of two masses m separated by a proper distance ℓ along the x_2 direction that are coupled by a lossy spring, the equation for the differential motion of the masses in the gravitational wave of the previous example becomes

$$\frac{d^2 x_{2R}}{dt^2} + \frac{\omega_o}{Q} \frac{dx_{2R}}{dt} + \omega_o^2 x_{2R} = c^2 R_{2020} \ell,$$

where x_{2R} is the proper relative displacement of the two masses, and R_{2020} is that component of the Riemannian curvature tensor which interacts with the masses to give relative displacements in the x_2 direction; it can be interpreted as a gravitational gradient force.

For the plane wave,

$$R_{2020} = \frac{1}{2c^2} \frac{d^2 h_{22}}{dt^2}$$

If the masses are free, the equation of differential motion becomes

$$\frac{d^2 x_{2R}}{dr^2} = \frac{1}{2} \frac{d^2 h_{22}}{dt^2} \ell$$

and, for zero-velocity initial conditions, the strain becomes $\frac{x_{2R}}{\ell} = \frac{1}{2} h_{22}$, which is the same result as that arrived at by the geometric approach.

The intensity of the gravitational wave in terms of the plane-wave metric tensor is given by Landau and Lifshitz[5] as

$$I_g = \frac{c^3}{16\pi G}\left[\left(\frac{dh_{23}}{dt}\right)^2 + \frac{1}{4}\left(\frac{dh_{22}}{dt} - \frac{dh_{33}}{dt}\right)^2\right]. \qquad (1)$$

3. Gravitational Radiation Sources – Weber Events and Limits on Pulsar Radiation

The strain that Weber observes in his bars is of the order of $\Delta\ell/\ell \sim 10^{-16}$. If the strain is caused by impulsive events that can excite a 1.6 kHz oscillation in the bars, the events must have a rise time of 10^{-3} second or less – the fact that the bars have a high Q does not enter into these considerations. The peak incident gravitational flux of these events is truly staggering. Using Eq. 1, we calculate $I_g \geq 5 \times 10^9$ erg/s/cm^2.

If the sources of this radiation, which are alleged to be at the center of the galaxy, radiate isotropically, each pulse carries at least 5×10^{52} ergs out of the galaxy, the equivalent of the complete conversion to gravitational energy of 1/40 of the sun's rest mass. Weber observes on the average one of these events per day. At this rate the entire known rest mass of the galaxy would be converted into gravitational radiation in 10^{10} years. Gravitational radiation would then become the dominant energy loss mechanism for the galaxy.

Gravitational radiation by pulsar NP 0532, even at best, is not expected to be as spectacular as the Weber pulses. Gold[6] and Pacini[7] have proposed that pulsars are rotating neutron stars with off-axis magnetic fields. In a neutron star the surface magnetic field can be so large ($\sim 10^{12}$-10^{13} G) that the magnetic stresses perceptibly distort the star into an ellipsoid with a principal axis along the magnetic moment of the star. The star, as viewed in an inertial coordinate system, has a time-dependent mass quadrupole moment that could be a source of gravitational radiation at twice the rotation frequency of the star. Gunn and Ostriker[8] have made a study of this pulsar model and conclude from the known lifetime and present decay of the rotation frequency of NP 0532 that no more than 1/6 of the rotational energy loss of the pulsar could be attributed to gravitational radiation. The measured and assumed parameters for NP 0532 are listed below.

Rotation Frequency	$\nu = 30.2155\ldots\ (\pm 3.4 \times 10^{-9})$ Hz
Slowdown Rate	$d\nu/dt = -3.859294 \pm .000053 \times 10^{-10}$ Hz/s
Distance	$d = 1.8$ kpc
Mass	$m = 1.4\ m_\odot$
Radius	$r = 10$ km.

The gravitational radiation intensity at 60.4 Hz incident on the Earth must be less than $I_g \leq 1 \times 10^{-6}$ erg/cm^2/s. The strain amplitude corresponding to this intensity is $\Delta\ell/\ell \leq 10^{-24}$.

4. Proposed Antenna Design

The principal idea of the antenna is to place free masses at several locations and measure their separations interferometrically. The notion is not new; it has appeared as a gedanken experiment in F. A. E. Pirani's[9] studies of the measurable properties of the Riemann tensor. However, the realization that with the advent of lasers it is feasible to detect gravitational waves by using this technique grew out of an undergraduate seminar that I ran at M.I.T. several years ago, and has been independently discovered by Dr. Philip Chapman of the National Aeronautics and Space Administration, Houston.

A schematic diagram of an electromagnetically coupled gravitational antenna is shown in Fig. V-20. It is fundamentally a Michelson interferometer operating in vacuum with the mirrors and beam splitter mounted on horizontal seismometer suspensions. The suspensions must have resonant frequencies far below the frequencies in the gravitational wave, a high Q, and negligible mechanical mode cross coupling. The laser beam makes multiple passes in each arm of the interferometer. After passing through the beam splitter, the laser beam enters either interferometer arm through a hole in the reflective coating of the spherical mirror nearest the beam splitter. The beam is reflected and refocused by the far mirror, which is made slightly astigmatic. The beam continues to bounce back and forth, hitting different parts of the mirrors, until eventually it emerges through another hole in the reflective coating of the near mirror. The beams from both arms are recombined at the beam splitter and illuminate a photodetector. Optical delay lines of the type used in the interferometer arms have been described by Herriott.[10] An experimental study of the rotational and transverse translational stability of this kind of optical delay line has been made by M. Wagner.[11]

The interferometer is held on a fixed fringe by a servo system which controls the optical delay in one of the interferometer arms. In such a mode of operation, the servo output signal is proportional to the differential strain induced in the arms. The servo signal is derived by modulating the optical phase in one arm with a Pockel-effect phase shifter driven at a frequency at which the laser output power fluctuations are small, typically frequencies greater than 10 kHz. The photo signal at the modulation frequency is synchronously detected, filtered, and applied to two controllers: a fast controller which is another Pockel cell optical phase shifter that holds the fringe at high frequencies, and a slow large-amplitude controller that drives one of the suspended masses to compensate for thermal drifts and large-amplitude low-frequency ground noise.

The antenna arms can be made as large as is consistent with the condition that the travel time of light in the arm is less than one-half the period of the gravitational wave

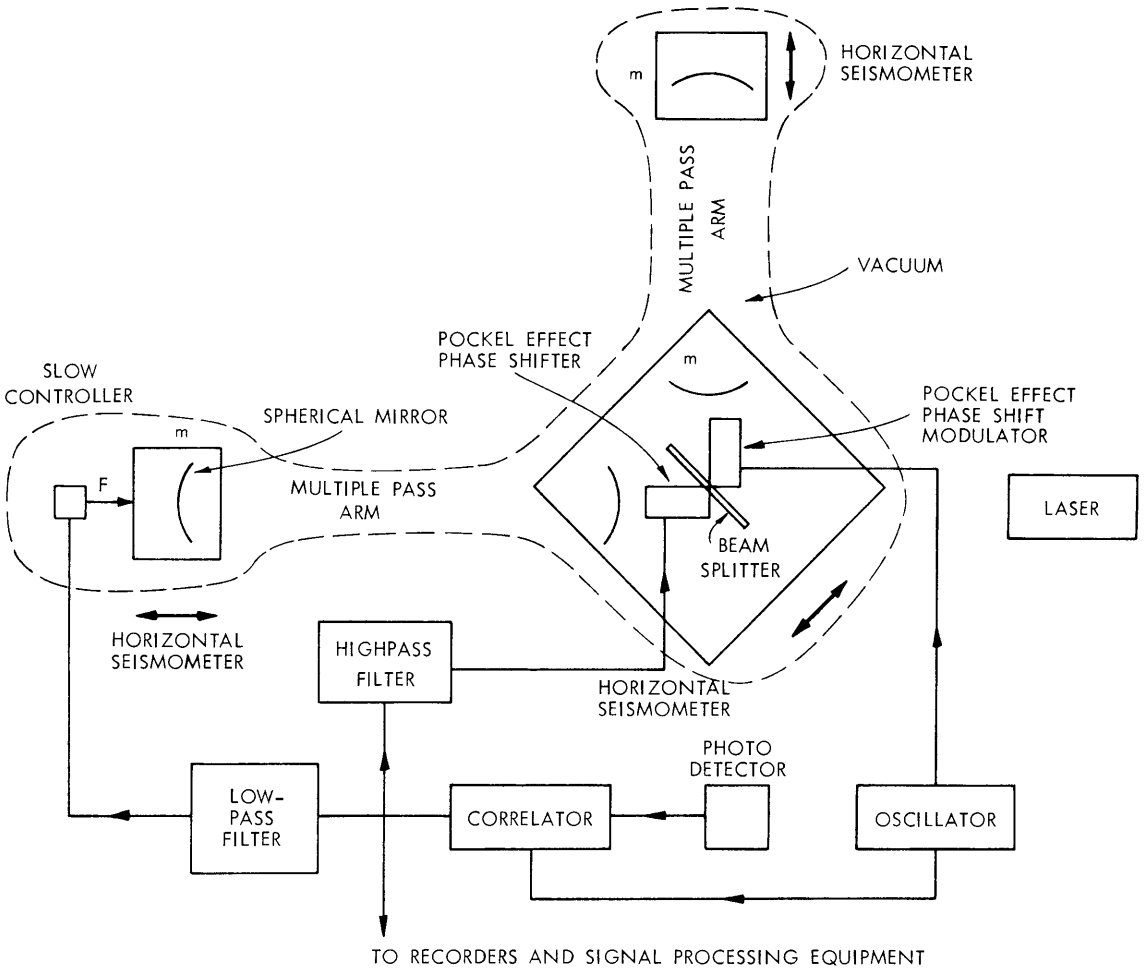

Fig. V-20. Proposed antenna.

that is to be detected. This points out the principal feature of electromagnetically coupled antennas relative to acoustically coupled ones such as bars; that an electromagnetic antenna can be longer than its acoustic counterpart in the ratio of the speed of light to the speed of sound in materials, a factor of 10^5. Since it is not the strain but rather the differential displacement that is measured in these gravitational antennas, the proposed antenna can offer a distinct advantage in sensivity relative to bars in detecting both broadband and single-frequency gravitational radiation. A significant improvement in thermal noise can also be realized.

5. Noise Sources in the Antenna

The power spectrum of noise from various sources in an antenna of the design shown in Fig. V-20 is estimated below. The power spectra are given in equivalent displacements squared per unit frequency interval.

a. Amplitude Noise in the Laser Output Power

The ability to measure the motion of an interferometer fringe is limited by the fluctuations in amplitude of the photo current. A fundamental limit to the amplitude noise in a laser output is the shot noise in the arrival rate of the photons, as well as the noise generated in the stochastic process of detection. At best, a laser can exhibit Poisson amplitude noise. This limit has been approached in single-mode gas lasers that are free of plasma oscillations and in which the gain in the amplifying medium at the frequency of the oscillating optical line is saturated.[12, 13]

The equivalent spectral-noise displacement squared per unit frequency interval in an interferometer of the design illustrated by Fig. V-20, illuminated by a Poisson noise-limited laser and using optimal signal processing, is given by

$$\frac{\Delta x^2(f)}{\Delta f} \geq \frac{hc\lambda}{8\pi^2 \epsilon P b^2 e^{-b(1-R)}},$$

where h is Planck's constant, c the velocity of light, λ the wavelength of the laser light, ϵ the quantum efficiency of the photodetector, P the total laser output power, b the number of passes in each interferometer arm, and R the reflectivity of the spherical mirrors. The expression has a minimum value for $b = 2/(1-R)$.

As an example, for a 0.5 W laser at 5000 Å and a mirror reflectivity of 99.5% using a photodetector with 50% quantum efficiency, the minimum value of the spectral noise power is

$$\frac{\Delta x^2(f)}{\Delta f} \geq 10^{-33} \text{ cm}^2/\text{Hz}.$$

b. Laser Phase Noise or Frequency Instability

Phase instability of the laser is transformed into displacement noise in an interferometer with unequal path lengths. In an ideal laser the phase noise is produced by spontaneous emission which adds photons of random phase to the coherent laser radiation field. The laser phase performs a random walk in angle around the noise-free phase angle given by $\phi_o = \omega_o t$. The variance in the phase grows as $(\overline{\Delta\phi})^2 = t/st_c$, where s is the number of photons in the laser mode, t_c the laser cavity storage time, and t the observation time. This phase fluctuation translates into an oscillating frequency width of the laser given by $\delta = 1/4\pi t_c s$.

Armstrong[14] has made an analysis of the spectral power distribution in the output of a two-beam interferometer illuminated by a light source in which the phase noise has a Gaussian distribution in time. By use of his results, the equivalent power spectrum

of displacement squared per unit frequency in the interferometer is given by

$$\frac{\Delta x^2(f)}{\Delta f} = \frac{4}{3}\lambda^2\delta^2\tau^3$$

for the case $f\tau \ll 1$ and $\delta\tau \ll 1$, where τ is the difference in travel time of light between the two paths in the interferometer.

The main reason for using a Michelson interferometer in the gravity antenna is that τ can be made small (equal to zero, if necessary), so that excessive demands need not be made on the laser frequency stability. In most lasers δ is much larger than that because of spontaneous emission, especially for long-term measurements (large τ). For small τ, however, δ does approach the theoretical limit. In a typical case δ might be of the order of 10 Hz and τ approximately 10^{-9} second, which gives

$$\frac{\Delta x^2(f)}{\Delta f} \leq 10^{-34}\ \text{cm}^2/\text{Hz}.$$

c. Mechanical Thermal Noise in the Antenna

Mechanical thermal noise enters the antenna in two ways. First, there is thermal motion of the center of mass of the masses on the horizontal suspensions and second, there is thermal excitation of the internal normal modes of the masses about the center of mass. Both types of thermal excitation can be handled by means of the same technique. The thermal noise is modeled by assuming that the mechanical system is driven by a stochastic driving force with a spectral power density given by

$$\frac{\Delta F^2(f)}{\Delta f} = 4kT\alpha \qquad \text{dyn}^2/\text{Hz},$$

where k is Boltzmann's constant, T the absolute temperature of the damping medium, and α the damping coefficient. We can express α in terms of Q, the resonant frequency, ω_o, of the mechanical system, and the mass. Thus $\alpha = m\omega_o/Q$. The spectral power density of the displacement squared, because of the stochastic driving force on a harmonic oscillator, is

$$\frac{\Delta x^2(f)}{\Delta f} = \frac{1}{m^2\omega_o^4}\,\frac{1}{(1-z^2)^2 + z^2/Q^2}\,\frac{4kT\omega_o m}{Q},$$

where $z = \omega/\omega_o$. The seismometer suspension should have a resonant frequency much lower than the frequency of the gravitational wave that is to be detected; in this case $z \gg 1$ and $Q \gg 1$, to give

$$\frac{\Delta x^2(f)}{\Delta f} = 4 \frac{\omega_o}{\omega^4} \frac{kT}{mQ}.$$

On the other hand, the lowest normal-mode frequencies of the internal motions of the masses, including the mirrors and the other suspended optical components, should be higher than the gravitational wave frequency. Some care must be taken to make the entire suspended optical system on each seismometer mount as rigid as possible. For the internal motions $z \ll 1$ and $Q \gg 1$, so that

$$\frac{\Delta x^2(f)}{\Delta f} = \frac{4kT}{\omega_o^3 mQ}.$$

It is clear that, aside from reducing the temperature, the thermal noise can be minimized by using high-Q materials and a high-Q suspension, as long as the gravitational wave frequency does not fall near one of the mechanical resonances. The range of Q for internal motions is limited by available materials: quartz has an internal Q of approximately 10^6, while for aluminum it is of the order of 10^5. The Q of the suspension can be considerably higher than the intrinsic Q of materials. The relevant quantity is the ratio of the potential energy stored in the materials to that stored in the Earth's gravitational field in the restoring mechanism.

The suspensions are critical components in the antenna, and there is no obvious optimal design. The specific geometry of the optics in the interferometer can make the interferometer output insensitive to motions along some of the degrees of freedom of the suspension. For example, the interferometer shown in Fig. V-20 is first-order insensitive to motions of the suspended masses transverse to the direction of propagation of light in the arms. It is also first-order insensitive to rotations of the mirrors. Motions of the beam splitter assembly along the 45° bisecting line of the interferometer produce common phase shifts in both arms and therefore do not appear in the interferometer output. Nevertheless, the success of the antenna rests heavily on the mechanical design of the suspensions because the thermal noise couples in through them, and they also have to provide isolation from ground noise.

The general problem with suspensions is that in the real world they do not have only one degree of freedom but many, and these modes of motion tend to cross-couple nonlinearly with each other, so that, by parametric conversion, noise from one mode appears in another. A rule of thumb, to minimize this problem in suspensions, is to have as few modes as possible, and to make the resonance frequencies of the unwanted modes high relative to the operating mode.[15]

It is still worthwhile to look at an example of the theoretical thermal noise limit of a single-degree-of-freedom suspension. If the internal Q is 10^5, the mass 10 kG, and

the lowest frequency resonance in the mass 10 kHz, the thermal noise from internal motions at room temperature for frequencies less than 10 kHz is

$$\frac{\Delta x^2(f)}{\Delta f} \sim 10^{-35} \text{ cm}^2/\text{Hz}.$$

The thermal noise from center-of-mass motion on the suspension for a $Q \sim 10^4$ and a resonant frequency of 5×10^{-2} Hz becomes

$$\frac{\Delta x^2(f)}{\Delta f} \sim \frac{10^{-24}}{f^4} \text{ cm}^2/\text{Hz}$$

for frequencies greater than the resonant frequency of the suspension. With the chosen sample parameters, the Poisson noise in the laser amplitude is larger than the thermal noise at frequencies greater than 200 Hz. An antenna that might be used in the pulsar radiation search would require, at room temperature, an mQ product 10^2 larger than the example given, to match the Poisson noise of the laser.

d. Radiation-Pressure Noise from the Laser Light

Fluctuations in the output power of the laser can drive the suspended masses through the radiation pressure of light. In principle, if the two arms of the interferometer are completely symmetric, both mechanically and optically, the interferometer output is insensitive to these fluctuations. Since complete symmetry is hard to achieve, this noise source must still be considered. An interesting point is that although one might find a high modulation frequency for the servo system where the laser displays Poisson noise, it is the spectral power density of the fluctuations in the laser output at the lower frequency of the gravitational wave which excites the antenna. In other words, if this is a serious noise source, the laser has to have amplitude stability over a wide range of frequencies.

Radiation-pressure noise can be treated in the same manner as thermal noise. If the laser displays Poisson noise, the spectral power density of a stochastic radiation-pressure force on one mirror is

$$\frac{\Delta F^2_{\text{rad}}(f)}{\Delta f} = \frac{4b^2 hP}{\lambda c} \qquad \text{dyn}^2/\text{Hz},$$

where b is the number of times the light beam hits the mirror, and P is the average total laser power. Using the same sample parameters for the suspension as we used in calculating the thermal noise, and those for the laser in the discussion of the amplitude noise, the ratio of stochastic radiation pressure forces relative to stochastic thermal forces is

$$\frac{\Delta F^2_{rad}(f)}{\Delta F^2_{thermal}(f)} \sim 10^{-6}.$$

e. Seismic Noise

If the antenna masses were firmly attached to the ground, the seismic noise, both through horizontal and tilt motions of the ground, would be larger than any of the other noise sources considered thus far. The seismic noise on the earth at frequencies higher than 5 Hz has been studied by several investigators[16-18] at various locations both on the surface and at different depths. In areas far from human industrial activity and traffic, the high-frequency noise can be characterized by a stationary random process. The noise at the surface appears higher than at depths of 1 km or more, but an unambiguous determination of whether the high-frequency noise is due to Rayleigh or to body waves has not been carried out. Measurements made in a zinc mine at Ogdensburg, New Jersey,[16] at a depth of approximately 0.5 km have yielded the smallest published values of seismic noise. In the region 10-100 Hz, the power spectrum is approximated by

$$\frac{\Delta x^2_\ell(f)}{\Delta f} \sim \frac{3 \times 10^{-14}}{f^4} \text{ cm}^2/\text{Hz}.$$

Although the spectrum has not been measured at frequencies higher than 100 Hz, it is not expected to decrease more slowly with frequency at higher frequencies. Surface measurements are typically larger by an order of magnitude.

By mounting the antenna masses on horizontal seismometer suspensions, we can substantially reduce the seismic noise entering the interferometer. The isolation provided by a single-degree-of-freedom suspension is given by

$$\left|\frac{\Delta x_m(f)}{\Delta x_\ell(f)}\right|^2 = \frac{\left[(1-z^2) + (2/Q)^2\right]^2 + (z^3/Q)^2}{\left[(1-z^2)^2 + (z/Q)^2\right]^2},$$

where $z = f/f_o$, and f_o is the resonant frequency of the suspension. $\Delta x_m(f)$ is the displacement of an antenna mass at frequency f relative to an inertial frame, and $\Delta x_\ell(f)$ is the motion of the Earth measured in the same reference frame.

At frequencies for which $z \gg 1$, the isolation ratio is

$$\left|\frac{\Delta x_m(f)}{\Delta x_\ell(f)}\right|^2 \sim \left(\frac{f_o}{f}\right)^4 + \left(\frac{f_o}{f}\right)^2 \frac{1}{Q^2}.$$

For the sample suspension parameters given, the estimated seismic noise entering

the antenna is

$$\frac{\Delta x^2(f)}{\Delta f} > \frac{2 \times 10^{-18}}{f^8} \text{ cm}^2/\text{Hz}; \quad 10 < f < 10 \text{ kHz}$$

with the average seismic driving noise at the Earth's surface assumed. For frequencies higher than 100 Hz, the effect of seismic noise is smaller than the noise from the laser amplitude fluctuations.

Although the isolation is adequate for detecting Weber-type events, an antenna to detect pulsar radiation would require better rejection of the ground noise. Several approaches are possible. Clearly, the suspension period can be increased to be longer than 20 s, but suspensions of very long periods are difficult to work with. Several shorter period suspensions may be used in series, since their isolation factors multiply. The disadvantage of this is that by increasing the number of moving members, the mode cross-coupling problem is bound to be aggravated.

An interesting possibility of reducing the seismic noise is to use a long-baseline antenna for which the period of the gravitational wave is much shorter than the acoustic travel time through the ground between the antenna end points. In this situation, the sections of ground at the end points are uncoupled from each other and the gravitational wave moves the suspended mass in the same way as the ground around it. In other words, there is little differential motion between the suspended mass and the neighboring ground because of the gravitational wave. Differential motion would result primarily from seismic noise. The differential motion can be measured by using the suspended mass as an inertial reference in a conventional seismometer. This information can be applied to the interferometer output to remove the seismic-noise component.

f. Thermal-Gradient Noise

Thermal gradients in the chamber housing the suspension produce differential pressures on the suspended mass through the residual gas molecules. The largest unbalanced heat input into the system occurs at the interferometer mirror where, after multiple reflections, approximately 1/10 of the laser power will be absorbed.

The excess pressure on the mirror surface is approximately $p \sim nk\Delta T$, where n is the number of gas molecules/cm^3, k is Boltzmann's constant, and ΔT is the difference in temperature between the mirror surface and the rest of the chamber. The fluctuations in ΔT can be calculated adequately by solving the one-dimensional problem of thermal diffusion from the surface into the interior of the mirror and the associated antenna mass, which are assumed to be at a constant temperature.

The mirror surface temperature fluctuations, $\Delta T(f)$, driven by incident intensity fluctuations $\Delta I(f)$, is given by

$$\Delta T(f) = \frac{\Delta I(f)}{4\epsilon\sigma T_o^3 + (\pi c_v \rho k_t)^{1/2} f^{1/2}} .$$

The first term in the denominator is the radiation from the surface, with ϵ the emissivity, σ the Stefan-Boltzmann constant, and T_o the ambient temperature. The second term is due to thermal diffusion from the surface into the interior, with c_v the specific heat, ρ the density, and k_t the thermal conductivity of the mirror.

If the laser exhibits Poisson noise, the spectral force density on the antenna mass becomes

$$\frac{\Delta F^2(f)}{\Delta f} = \frac{2(nk)^2}{f(\pi c_v \rho k_t)} \frac{hc}{\lambda} \overline{P} \qquad \text{dyn}^2/\text{Hz}.$$

Radiation is neglected because it is much smaller than the thermal diffusion. Using the following parameters for glass, $c_v \sim 10^6$ erg/gm °K, $\rho \sim 4$, $k_t \sim 10^3$ erg/s cm °K, an average laser power of 0.5 W and a vacuum of 1×10^{-8} mm Hg, the ratio of the thermal-gradient noise to the thermal noise forces in the sample suspension is

$$\frac{\Delta F^2_{T,G}(f)}{\Delta F^2_{th}(f)} \sim \frac{10^{-15}}{f} .$$

g. Cosmic-Ray Noise

The principal component of the high-energy particle background both below and on the Earth's surface is muons with kinetic energies[19] greater than 0.1 BeV. A muon that passes through or stops in one of the antenna masses imparts momentum to the mass, thereby causing a displacement that is given by

$$\Delta x = \frac{\Delta E \cos\theta}{m\omega_o c},$$

where ΔE is the energy loss of the muon in the antenna mass, θ the angle between the displacement and the incident muon momentum, m the antenna mass, and ω_o the suspension resonant frequency.

The energy loss of muons in matter is almost entirely through electromagnetic interactions so that the energy loss per column density, k(E), is virtually constant with energy for relativistic muons. A 10^{-1} BeV muon loses 3 MeV/gm/cm^2, while a 10^4 BeV muon loses ~30 MeV/gm/cm^2.

The vertical flux of muons at sea level with an energy greater than 10^{-1} BeV is approximately 10^{-2} particles/cm^2 sec sr. For energies larger than 10 BeV, the

integrated flux varies as $\sim 10^{-1}/E^2$(BeV).

Since the flux falls off steeply with energy and the energy loss is almost independent of energy, the bulk of the muon events will impart the same momentum to the suspension. If we use the following sample suspension parameters, $m \sim 10^4$ g, $f_o \sim 5 \times 10^{-2}$ Hz, $\rho \sim 3$, and typical linear dimensions ~10 cm, the average energy loss per muon is $\sim 10^{-1}$ BeV. At sea level the antenna mass might experience impulsive displacements of $\sim 10^{-18}$ cm occurring at an average rate of once a second. An event arising from the passage of a 10^4 BeV muon results in a displacement of 10^{-17} cm at a rate of once a year.

Although the shape of the antenna mass can be designed to reduce somewhat the effect and frequency of muon interactions especially if we take advantage of the anisotropy of the muon flux, the best way of reducing the noise is to place the antenna masses underground. The pulse rate at depths of 20 m, 200 m, and 2 km is approximately 3×10^{-2}, 10^{-4}, 10^{-9} pulses/second.

If the antenna output is measured over times that include many muon pulses, as it would be in a search for pulsar radiation, the noise can be treated as a stationary distribution. Under the assumption that the muon events are random and, for ease of calculation, that the magnitude of the momentum impacts is the same for all muons, the spectral power density of displacement squared of the antenna mass is

$$\frac{\Delta x^2(f)}{\Delta f} = \frac{4N(\Delta E/c)^2}{(2\pi)^4 m^2 f^4} \qquad \text{cm}^2/\text{Hz}$$

for $f \gg f_o$, where N is the average number of pulses per second, $\Delta E/c$ the momentum imparted to the mass per pulse, and m the antenna mass. For the sample suspension parameters at sea level

$$\frac{\Delta x^2(f)}{\Delta f} \sim 10^{-40}/f^4 \qquad \text{cm}^2/\text{Hz}.$$

h. Gravitational-Gradient Noise

The antenna is sensitive to gravitational field gradients, that is, differential gravitational forces exerted on the masses defining the ends of the interferometer arms. No data are available concerning high-frequency gravitational gradients that occur naturally on or near the surface of the earth. Two effects can bring about gravitational-gradient noise: first, time-dependent density variations in both the atmosphere and the ground, and second, motions of existing inhomogeneities in the mass distribution around the antenna.

An estimate of these two effects can be made with a crude model. Assume that one of the antenna masses is at the boundary of a volume that has a fluctuating density. The

amount of mass that can partake in a coherent density fluctuation at frequency f and exert a force on the mass is roughly that included in a sphere with a radius equal to half the acoustic wavelength, λ, in the ground. The fluctuating gravitational force on the mass is

$$\frac{F_g(f)}{m} \sim \frac{2}{3}\,\pi\lambda\Delta\rho(f)\,G,$$

where $\Delta\rho(f)$ is the density fluctuation at frequency f, and G the Newtonian gravitational constant. The density fluctuations driven by ground noise in the sphere are

$$\Delta\rho(f) = 3\langle\rho\rangle\,\frac{\Delta x_e(f)}{\lambda},$$

where $\langle\rho\rangle$ is the average density of the ground, and $\Delta x_e(f)$ is the ground noise displacement. If f is larger than the resonant frequency of the suspension, the ratio of the displacement squared of the mass to that of the ground motion is given by

$$\frac{\Delta x_m^2(f)}{\Delta x_e^2(f)} = \left[\frac{\langle\rho\rangle G}{2\pi f^2}\right]^2.$$

For the earth, this isolation factor is

$$\frac{\Delta x_m^2(f)}{\Delta x_e^2(f)} \sim \frac{10^{-14}}{f^4},$$

which is much smaller than the isolation factor for the attenuation of direct ground motion by the sample suspension.

A comparable approach can be used in estimating the effect of motions of inhomogeneities in the distribution of matter around the antenna which are driven by ground noise. If we assume an extreme case of a complete inhomogeneity, for example, an atmosphere-ground interface, the mass that partakes in a coherent motion, $\Delta x(f)$, could be $m \sim \lambda^3\langle\rho\rangle$. The fluctuating force on the nearest antenna mass is

$$\frac{F_g(f)}{m} = \frac{2}{3}\,\pi G\langle\rho\rangle\,\Delta x(f).$$

The isolation factor is

$$\frac{\Delta x_m^2(f)}{\Delta x_e^2(f)} \sim \left[\frac{G\langle\rho\rangle}{6\pi f^2}\right]^2,$$

which is comparable to the isolation factor attributable to density fluctuations. These factors become smaller if the distance between the masses is less than λ.

i. Electric Field and Magnetic Field Noise

Electric fields in dielectric-free conducting vacuum chambers are typically 10^{-3} V/cm. These fields result from variations in the work function of surfaces and occur even when all surfaces in a system are constructed of the same material, since the work function of one crystal face is different from that of another. Temporal fluctuations in these fields are caused by impurity migrations and variations in adsorbed gas layers. Little is known about the correlation time of these fluctuations, except that at room temperature it seems to be longer than a few seconds and at cryogenic temperatures it is possible to keep the fields constant to better than 10^{-12} V/cm for several hours.[20]

The electric force on a suspended antenna mass is

$$F_e \sim \frac{1}{4\pi} \mathscr{E}^2 A,$$

where A is the exposed antenna surface, and $\mathscr{E}$ is the fluctuating electric field at the surface. Under the assumption that the power spectrum of the field fluctuations is similar to that of the flicker effect in vacuum tubes or to the surface effects in semiconductors, both of which come from large-scale, but slow, changes in the surface properties of materials, the electric force power spectrum might be represented by

$$\frac{\Delta F_e^2(f)}{\Delta f} \sim \frac{\frac{2}{\pi}\langle F_e^2\rangle \, 1/\tau_o}{(1/\tau_o)^2 + (2\pi f)^2} \qquad \text{dyn}^2/\text{Hz},$$

where τ_o is the correlation time of the fluctuations, and $\langle F_e^2\rangle$ is the average electric force squared.

If the gravitational wave frequency is much greater than $1/\tau_o$ and also higher than the resonant frequency of the suspension, the power spectrum of the displacements squared becomes

$$\frac{\Delta x^2(f)}{\Delta f} = \frac{\langle \mathscr{E}^4\rangle A^2}{32\pi^6 m^2 \tau_o f^4} \qquad \text{cm}^2/\text{Hz}.$$

For $m \sim 10^4$ gm, $A \sim 10^2$ cm^2, $\mathscr{E} \sim 10^{-5}$ stat V/cm and $\tau_o \sim 1$ s,

$$\frac{\Delta x^2(f)}{\Delta f} \sim 10^{-38}/f^4 \qquad \text{cm}^2/\text{Hz}.$$

This noise is considerably less than that from the Poisson noise of the laser. Nevertheless, it is necessary to take care to shield, electrostatically, the deflection mirror surfaces.

Geomagnetic storms caused by ionospheric currents driven by the solar wind and cosmic rays create fluctuating magnetic fields at the surface of the Earth. The smoothed power spectrum of the magnetic field fluctuations in mid-latitude regions at frequencies greater than 10^{-3} Hz is approximately[21]

$$B^2(f) \sim B_o^2/f^2 \qquad G^2/Hz,$$

with $B_o \sim 3 \times 10^{-8}$ G. Large pulses with amplitudes $\sim 5 \times 10^{-3}$ G are observed occasionally; the rise time of these pulses is of the order of minutes.[22]

Fluctuating magnetic fields interact with the antenna mass primarily through eddy currents induced in it or, if it is constructed of insulating material, in the conducting coating around the antenna that is required to prevent charge buildup. The interaction, especially at low frequencies, can also take place through ferromagnetic impurities in nonmagnetic materials. Magnetic field gradients cause center-of-mass motions of the suspended mass. Internal motions are excited by magnetic pressures if the skin depth is smaller than the dimensions of the antenna mass.

In an extreme model it would be assumed that the fluctuating magnetic fields are completely excluded by the antenna mass and that the field changes over the dimensions of the mass are equal to the fields. The magnetic forces are $F_m = \frac{1}{4\pi} B^2 A$.

The power spectrum for center-of-mass motions, with $f \gg f_o$, becomes

$$\frac{\Delta x^2(f)}{\Delta f} = \frac{A^2 B_o^4}{16\pi^3 m^2 f^4} \qquad cm^2/Hz.$$

For the sample suspension, using the smoothed power spectrum of magnetic field fluctuations, we have

$$\Delta x^2(f) \sim 10^{-36}/f^4 \qquad cm^2/Hz.$$

The displacements arising from internal motions driven by magnetic pressures at frequencies lower than the internal resonant frequency, $f_{o_{int}}$, are given by

$$\frac{\Delta x^2(f)}{\Delta f} = \frac{A^2 B_o^4}{16\pi^3 m^2 f_{o_{int}}^2 f^2} \qquad cm^2/Hz.$$

Although the disturbances caused by the smoothed power spectrum do not appear

troublesome in comparison with the other noise sources, the occasional large magnetic pulses will necessitate placing both conducting and high-μ magnetic shields around the antenna masses. (It is not inconceivable that Weber's coincident events may be caused by pulses in geomagnetic storms, if his conducting shielding is inadequate. It would require a pulse of 10^{-2} G with a rise time $\sim 10^{-3}$ s to distort his bars by $\Delta\ell/\ell \sim 10^{-16}$.)

6. Detection of Gravitational Waves in the Antenna Output Signal

The interferometer (servo) output signal is filtered after detection. The gravitational wave displacements in the filtered output signal are given by

$$\Delta x_g^2 = \frac{1}{4} \int_o^\infty |F(f)|^2 \, h^2(f) \, \ell^2 \, df,$$

where $F(f)$ is the filter spectral response, $h^2(f)$ is the spectral power density of the gravitational wave metric components, and ℓ is the arm length of the antenna interferometer. The noise displacements in the filtered output signal are given by

$$\Delta x_n^2 = \int_o^\infty |F(f)|^2 \frac{\Delta x_n^2(f)}{\Delta f} \, df,$$

where $\Delta x_n^2(f)/\Delta f$ is the spectral power density of the displacement noise. In order to observe a gravitational wave, the signal-to-noise ratio has to be greater than 1. That is, $\Delta x_g^2/\Delta x_n^2 > 1$.

The dominant noise source for the antenna appears to be the amplitude fluctuations in the laser output power. When translated into equivalent displacement of the masses, the noise has been shown to have a flat spectrum given by $\Delta x_n^2(f)/\Delta f \sim 10^{-33}$ cm^2/Hz.

If we assume this noise and an idealized unity gain bandpass filter with cutoff frequencies f_2 and f_1, then the signal-to-noise ratio becomes

$$\frac{\Delta x_g^2}{\Delta x_n^2} = \frac{1/4 \int_{f_1}^{f_2} h_2(f) \, \ell^2 \, df}{\frac{\Delta x_n^2(f)}{\Delta f} (f_2 - f_1)}.$$

For continuous gravitational waves, the minimum detectable gravitational wave metric spectral density is then

$$h^2(f) > \frac{4}{\ell^2} \frac{\Delta x_n^2(f)}{\Delta f} \approx \frac{4 \times 10^{-33}}{\ell^2(\text{cm})} \qquad \text{Hz}^{-1}.$$

Detectability criteria for pulses cannot be so well defined; a reasonable assumption

is that the pulse "energy" be equal to the noise "energy." The optimum filter should have a bandwidth comparable to the pulse bandwidth. The spectral density of a pulse of duration τ is roughly distributed throughout a $1/\tau$ bandwidth. A possible signal-to-noise criterion for pulses is then

$$\Delta x_g^2 \tau > \frac{\Delta x_n^2(f)}{\Delta f},$$

or in terms of h,

$$h^2 \tau > \frac{4}{\ell^2} \frac{\Delta x_n^2(f)}{\Delta f}.$$

As an example, the Weber pulses induce impulsive strains of $h \sim 2 \times 10^{-16}$ for a duration of approximately 10^{-3} s, so that $h^2\tau \sim 4 \times 10^{-35}$. A 1-m interferometer arm antenna of the proposed design would have a noise "energy" of 4×10^{-37}, so that the signal-to-noise ratio for Weber events would approach 100/1.

A meaningful search for the pulsar radiation requires a more elaborate and considerably more expensive installation. The spectral density of the pulsar gravitational wave metric is

$$h^2(f) = h_o^2 \delta(f-f_p),$$

where f_p is a multiple of the pulsar rotation frequency. The signal-to-noise ratio is

$$\frac{\Delta x_g^2}{\Delta x_n^2} = \frac{1/4\ h_o^2 \ell^2}{\frac{\Delta x_n^2}{\Delta f}(f_2-f_1)}.$$

By coherent amplitude detection, using a reference signal at multiples of the pulsar rotation frequency, we can reduce the filter bandwidth by increasing the postdetection integration time. The integration time, t_{int}, required to observe the pulsar radiation with a signal-to-noise ratio greater than 1 is given by

$$t_{int} > \frac{4 \frac{\Delta x_n^2(f_p)}{\Delta f}}{h_o^2 \ell^2}.$$

Assuming the Gunn-Ostriker upper limit for the gravitational radiation of the Crab Nebula pulsar, $h_o \sim 2 \times 10^{-24}$, and an antenna with a 1-km interferometer arm, we find that the integration time is around one day.

An interesting point, suggested by D. J. Muehlner, is that the Weber events, if they are gravitational radiation pulses, could constitute the dominant noise in a pulsar radiation search. Under the assumption that the Weber pulses cause steplike strains, h_o, at an average rate of n per second, and that the integration time includes many pulses, the power spectrum of displacement squared is given roughly by

$$\frac{\Delta x^2(f)}{\Delta f} \sim \frac{N\ell^2 h_o^2}{16\pi^2 f^2} \qquad \text{cm}^2/\text{Hz}.$$

With f ~ 60 Hz, $h_o \sim 10^{-16}$, $\ell \sim 10^5$ cm, and $N \sim 10^{-5}$/s, the noise is $\sim 10^{-32}$ cm^2/Hz, which is greater than the Poisson noise of the laser. Large pulses can be observed directly in the broadband output of the antenna and can therefore be removed in the data analysis of the pulsar signal. If the energy spectrum of gravitational radiation pulses is, however, such that there is a higher rate for lower energy pulses, in particular, if Nh_o^2 is constant as h_o gets smaller, gravitational radiation may prove to be the dominant noise source in the pulsar radiation measurements.

Appendix

Comparison of Interferometric Broadband and Resonant Bar Antennas for Detection of Gravitational Wave Pulses

Aside from their greater possible length, interferometric broadband antennas have a further advantage over bars, in that the thermal noise in the detection bandwidth for the gravitational wave pulse is smaller than for the bar. In the following calculation it is assumed that the thermal noise is the dominant noise in both types of antennas.

Let the gravitational radiation signal be a pulse given by

$$h(t) = \begin{cases} 0 & t < 0 \\ h & 0 \leq t \leq t_o \\ 0 & t > t_o \end{cases}$$

The spectral energy density of the pulse is

$$h^2(\omega) = \frac{2h^2 t_o^2}{(2\pi)^2} \frac{\sin^2 \omega t_o/2}{(\omega t_o/2)^2} \qquad 0 \leq \omega < \infty$$

$$\simeq \begin{cases} \dfrac{2h^2 t_o^2}{(2\pi)^2} & 0 < \omega \leq \pi/t_o \\ 0 & \omega > \pi/t_o \end{cases} \qquad \text{the equivalent energy box spectrum}$$

The gravitational force spectral density is

$$F_g^2(\omega) = \frac{1}{4}\omega^4 h^2(\omega)\, \ell^2 m^2.$$

Using the dynamic interpretation for the interaction of the bar with the gravitational-wave pulse, the "energy" in the bar after the pulse excitation is given by

$$\int_0^\infty x_g^2(t)\, dt = E_g = \frac{h^2 t_o^2 \ell^2 \omega_o Q}{4\pi} \qquad Q \gg 1, \quad \frac{\pi}{t_o} > \omega_o,$$

where ω_o is the resonant frequency of the bar.

The pulse "energy" is distributed throughout the ringing time of the bar so that

$$E_g \sim x_g^2(t)\, 2Q/\omega_o,$$

and the average displacement of the ends of the bar becomes

$$x_g^2(t) \sim \frac{h^2 t_o^2 \omega_o^2 \ell^2}{8\pi}.$$

The average thermal-noise displacement is

$$\langle x_{TH}^2 \rangle \sim \frac{4kT}{m\omega_o^2}.$$

The thermal noise also rings on the average for a period $\tau \sim 2Q/\omega_o$.

The signal-to-noise ratio for the bar is given by

$$\frac{x_g^2}{\langle x_{TH}^2 \rangle} \sim \frac{h^2 \ell^2 (t_o \omega_o)^2\, m\omega_o^2}{32\pi kT}.$$

Now make the same calculation for the broadband antenna with a filter matched to the pulse spectrum. The displacement spectrum is

$$x^2(\omega) = h^2(\omega)\, \ell^2 = \frac{2h^2 t_o^2 \ell^2}{(2\pi)^2}.$$

The pulse "energy" in a filter with matched bandwidth and a low-frequency cutoff ω_L is

$$E_g = 2\pi \int_{\omega_L}^{\pi/t_o} x^2(\omega)\, d\omega \cong \ell^2 h^2 t_o \qquad \omega_L \ll \pi/t_o.$$

If the resonant frequency, ω_o, of the suspension is smaller than ω_L, and the suspension has a high Q, the thermal "energy" in the same bandwidth is given by

$$E_{TH} = \langle x_{TH}^2 \rangle\, t_o = t_o \int_{\omega_L}^{\pi/t_o} \frac{1}{m^2\omega^4} \frac{4kT\omega_o m}{Q}\, d\omega.$$

Generally $\omega_L \ll \frac{\pi}{t_o}$, the thermal "energy" becomes

$$E_{TH} \sim \frac{4kT\omega_o t_o}{3Qm\omega_L^3}.$$

The signal-to-noise ratio for the broadband antenna is

$$\frac{E_g}{E_{TH}} = \frac{x_g^2}{\langle x_{TH}^2 \rangle} = \frac{3h^2\ell^2 Qm\omega_L^3}{4kT\omega_o}.$$

The signal-to-noise ratio for the broadband antenna relative to the equivalent-length resonant bar antenna at the same temperature is

$$R = \frac{(S/N)_{BB}}{(S/N)_B} = \frac{24\pi Q_{BB} m_{BB} \omega_L^3/\omega_{oBB}}{(t_o\omega_{oB})^2\, m_B \omega_{oB}^2}.$$

The best case for the bar is a pulse with $t_o \sim \frac{\pi}{\omega_o}$. If we assume Weber bar parameters $m_B \sim 10^6$ g, $\omega_{oB} \sim 10^4$ and the sample suspension parameters previously given, $Q_{BB} \sim 10^4$, $m_{BB} \sim 10^4$ g, $\omega_L \sim 10^3$, $\omega_{oBB} \sim 3 \times 10^{-1}$, the signal-to-noise ratio approaches $\sim 10^4$. This entire factor cannot be realized because the laser amplitude noise dominates in the interferometric antenna.

R. Weiss

References

1. A. Einstein, Sitzber. deut. Akad. Wiss. Berlin, Kl. Math. Physik u. Tech. (1916), p. 688; (1918), p. 154.
2. J. Weber, Phys. Rev. Letters 22, 1320 (1969).
3. J. Weber, Phys. Rev. Letters 25, 180 (1970).

4. J. Weber, Phys. Rev. 117, 306 (1960).

5. L. D. Landau and E. M. Lifshitz, The Classical Theory of Fields (Pergamon Press, London and New York, 1962).

6. T. Gold, Nature 218, 731 (1968).

7. F. Pacini, Nature 219, 145 (1968).

8. J. P. Ostriker and J. E. Gunn, Astrophys. J. 157, 1395 (1969).

9. F. A. E. Pirani, Acta. Phys. Polon. 15, 389 (1956).

10. D. R. Herriott and H. J. Schulte, Appl. Opt. 4, 883 (1965).

11. M. S. Wagner, S.B. Thesis, Department of Physics, M.I.T., June 1971 (unpublished).

12. G. Blum and R. Weiss, Phys. Rev. 155, 1412 (1967).

13. G. F. Moss, L. R. Miller, and R. L. Forward, Appl. Opt. 10, 2495 (1971).

14. J. A. Armstrong, J. Opt. Soc. Am. 56, 1024 (1966).

15. R. Weiss and B. Block, J. Geophys. Res. 70, 5615 (1965).

16. B. Isacks and J. Oliver, Bull. Seismol. Soc. Am. 54, 1941 (1964).

17. G. E. Frantti, Geophys. 28, 547 (1963).

18. E. J. Douze, Bull. Seismol. Soc. Am. 57, 55 (1967).

19. M. G. K. Menon and P. V. Ramana Murthy, in Progress in Elementary Particle and Cosmic Ray Physics, Vol. 9 (North-Holland Publishing Co., Amsterdam, 1967).

20. F. C. Witteborn and W. M. Fairbank, Phys. Rev. Letters 19, 1049 (1967).

21. W. H. Campbell, Ann. Geophys. 22, 492 (1966).

22. T. Sato, Rep. Ionosphere Space Res. Japan 16, 295 (1962).